AFCRL-68-0666
DECEMBER 1968
AIR FORCE SURVEYS IN GEOPHYSICS, NO. 208

AIR FORCE CAMBRIDGE RESEARCH LABORATORIES
L. G. HANSCOM FIELD, BEDFORD, MASSACHUSETTS

CORPUSCULAR RADIATION: A Revision of Chapter 17, Handbook of Geophysics and Space Environments

R.C. FILZ
L. KATZ
G.A. KUCK
M.A. SHEA
D.F. SMART

OFFICE OF AEROSPACE RESEARCH
United States Air Force

AFCRL-68-0666
DECEMBER 1968
AIR FORCE SURVEYS IN GEOPHYSICS, NO. 208

ENVIRONMENTAL CONSULTATION SERVICE

AIR FORCE CAMBRIDGE RESEARCH LABORATORIES

L. G. HANSCOM FIELD, BEDFORD, MASSACHUSETTS

CORPUSCULAR RADIATION: A Revision of Chapter 17, Handbook of Geophysics and Space Environments

R.C. FILZ
L. KATZ
G.A. KUCK
M.A. SHEA
D.F. SMART

OFFICE OF AEROSPACE RESEARCH

United States Air Force

Abstract

This survey is a summary of available information on the corpuscular radiation environment in the vicinity of the earth and in the earth's atmosphere; radiation trapped in the magnetosphere (Van Allen belts), galactic cosmic rays, and high-energy solar particles (solar cosmic rays) are described. The topics presented are: the motions of charged particles in the geomagnetic field; the spatial and temporal distributions, intensities, and energies of electrons and protons trapped in the earth's magnetic field; the composition, intensity, energy spectrum and variations of galactic cosmic rays; and the composition, intensities, anisotropy, and variations of the high-energy charged-particles emitted sporadically by the sun in association with solar flares and other solar disturbances.

Contents

Illustrations

Illustrations

Tables

Preface

This report is a revision of Sections 17.2 through 17.5 of Chapter 17 "Corpuscular Radiation" of the Handbook of Geophysics and Space Environments*; changes in Section 17.1 are minor. (Numbers of Sections are the same as those in the original Handbook so that the cross-referencing system in other chapters remains valid.) This survey represents the state of the art in June, 1968, when the manuscript was submitted.

SHEA L. VALLEY
Scientific Editor
Handbook of Geophysics and Space Environments

* Published by the Air Force Cambridge Research Laboratories and by the McGraw-Hill Book Co. in 1965.

Corpuscular Radiation : A Revision of Chapter 17, Handbook of Geophysics and Space Environments

This chapter outlines current knowledge of corpuscular radiation in the vicinity of earth; this includes the charged particles trapped in the geomagnetic field, cosmic radiation, and high-energy solar particles associated with solar flares. The sources, acceleration mechanisms, diffusion through space, and solar modulation processes are not well understood. The prediction of the occurrence of high-energy solar particle emission and of the characteristics of corpuscular radiation emitted during solar flare events is still an unsolved problem.

17.1 BASIC RELATIONS

17.1.1 Nomenclature and Definitions

Corpuscular radiation is usually characterized by the energy of the particle in electron volts. (The international symbol for 10^9 eV, now adopted by the U.S. Bureau of Standards, is GeV, rather than BeV.) The total energy is the sum of the kinetic energy, E_k, plus rest-mass energy,

$$E_T = E_k + m_o c^2 = mc^2, \tag{17-1}$$

(Received for publication 2 December 1968)

where m_o is the rest mass, m the relativistic mass, and c the speed of light in vacuo. For the proton, $m_o c^2$ is 938 MeV; for the electron, $m_o c^2$ is 0.511 MeV. It is customary in the literature to give values of the energy per nucleon for heavier particles.

The total energy is related to the particle momentum, p, by

$$E_T = (p^2c^2 + m_o^2c^4)^{1/2} . \tag{17-2}$$

In the absence of electric fields and of time-varying magnetic fields, E_T and p are constants of the particle's motion. In cosmic ray physics the momentum is often given in units of eV/c.

Observations of the intensity of corpuscular radiation are reported in various units depending upon the detection method. The unidirectional differential intensity, J(E), is the flux (number per unit time) of particles of a given energy per unit energy interval in a unit solid angle about the direction of observation, incident on a unit area perpendicular to the direction of observation; the units are usually particles $cm^{-2} s^{-1} sr^{-1} MeV^{-1}$. Unidirectional integral intensity, J (> E), is the intensity of particles with energy greater than a threshold energy, E,

$$J(>E) = \int_E^\infty J(E)dE. \tag{17-3}$$

Omnidirectional intensities are J(E), or J(>E), integrated over 4π solid angle.

The differential energy spectrum is J(E) plotted against E. The integral energy spectrum is J (>E) plotted against E. J(E) and J(>E) sometimes can be expressed as a power law;

$$J(E) = J_o E^{-\gamma} , \tag{17-4}$$

$$J(>E) = J_o(\gamma - 1)^{-1} E^{-\gamma+1} , \tag{17-5}$$

where $\gamma > 1$. It is also convenient sometimes to use an exponential law;

$$J(E) = J_o \exp(-E/E_o), \tag{17-6}$$

$$J(>E) = J_o E_o \exp(-E/E_o) \tag{17-7}$$

where E_o is defined as the average particle energy if the spectrum is of this simple exponential form.

Observations of counts per unit time or of ionization rates are often difficult to interpret and convert to J(E) or J (>E). When considerations of the effects of corpuscular radiation on personnel are of primary concern, intensities or counting rates must be converted to dose or dose rates. The rad is the unit of absorbed dose; one rad is 100 erg absorbed per gram of absorbing material. Conversion of observed particle fluxes to absorbed dose rate, however, is not straightforward and is sometimes impossible for lack of necessary details; the conversion depends in a complex way on the energies and kinds of particles and on geometrical configurations of the absorbers and direction of the incident beam, as well as on the different absorbing properties of materials.

The magnetic rigidity, P, of a particle is a measure of its resistance to a magnetic force that deflects the particle from a straight-line trajectory. The rigidity is defined as

$$P = pc/q \,, \tag{17-8}$$

where q is the charge of the particle. If pc is in electron volts, then q is the number of electronic charge units and P is in volts.

Figure 17-1 shows the relation between the rigidity of protons and alpha particles and their kinetic energy per nucleon; in using this figure for conversion of units, note that the energy scale must be multiplied by 4 (the number of nucleons) to obtain the total kinetic energy of an alpha particle.

On many occasions the magnetic rigidity is used in place of the kinetic energy in describing the flux spectrum. In particular, in lieu of Eq. 17-6, a frequently used expression is:

$$J(P) = J_o \exp(-P/P_o) \tag{17-9}$$

The geomagnetic field acts on cosmic rays as a magnetic analyzer, removing low rigidity charged particles from the flux incident at the top of the earth's atmosphere; particles of progressively lower rigidity are detected as the distance north or south of the geomagnetic equator increases. The cutoff or threshold rigidity of cosmic rays is the minimum rigidity that permits a charged particle to arrive from a specified direction at a given latitude and longitude; particles of lower rigidity are not observed at the specified location and direction because of this geomagnetic cutoff.

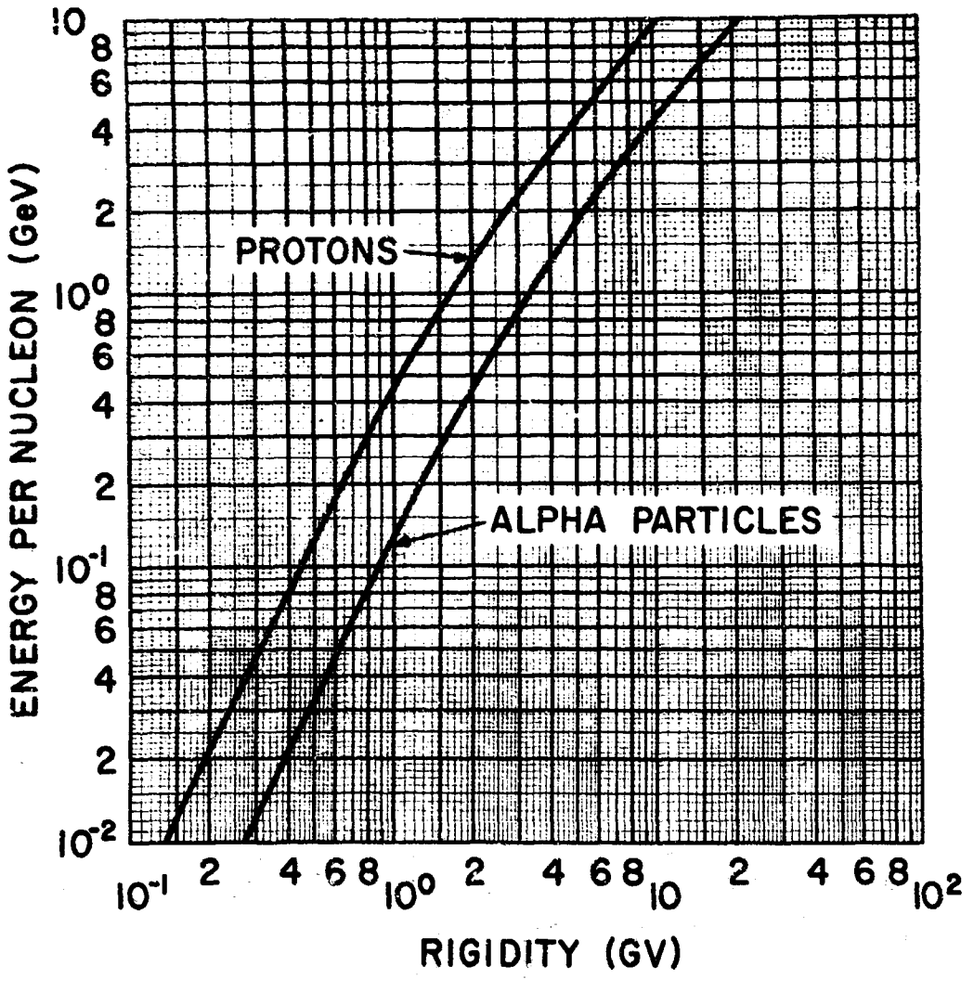

Figure 17-1. Conversion From Magnetic Rigidity to Kinetic Energy per Nucleon for Protons and Alpha Particles. Because nuclei heavier than He^3 have about the same charge to mass ratio as alpha particles (0.5), the alpha-particle curve also gives approximate values for the heavier nuclei

At a given location on the surface of the earth, only those cosmic ray particles that arrive from certain specific directions with respect to the station can be detected. These allowed directions form the asymptotic cone of acceptance; for asymptotic cones of acceptance of various cosmic-ray stations see McCracken, et al (1965).

17.1.2 Trapped Particle Motion in a Magnetic Field

Figure 17-2 illustrates the motion of a charged particle trapped in a magnetic dipole field. The particle is confined to the surface of a tube of magnetic lines of force, moving in a quasi-helical path with a rotational period τ_1, and oscillating back and forth between mirror points with a period τ_2. The pitch angle, α, is the angle between the momentum vector, p, and the magnetic vector, B; at the mirror point, α is 90^o. The particle also drifts slowly around the earth with an azimuthal drift period τ_3; negative particles drift to the east, positive particles to the west. In the geomagnetic field the orders of magnitude of the periods are: τ_1 for electrons, 10^{-6} s; τ_1 for protons, 10^{-3} s; τ_2 for electrons and protons, 1 s; τ_3 for electrons and protons, 10^3 s.

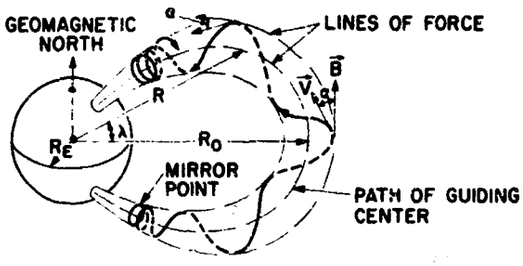

Figure 17-2. Diagram of the Simplified Motion of a Charged Particle Trapped in a Magnetic Dipole field; Azimuthal Drift is Ignored. $\vec{V}$ is the particle velocity, $\vec{B}$ the magnetic vector of the dipole field, and α is the pitch angle. (After Singer and Lenchek, 1962.)

The period τ_1 is the reciprocal of the gyrofrequency (cyclotron frequency). τ_1 is $2\pi m/qB$ or $2\pi E_T/c^2qB$ in Système International (MKSA); in Gaussian (mixed CGS) units, τ_1 is $2\pi E_T/cqB$. The radius of gyration, r_g, is $p(\sin\alpha)/qB$; in Gaussian units, r_g is $pc(\sin\alpha)/qB$. Because geomagnetic lines of force converge toward the poles, the particle penetrates regions of increasing magnetic flux density as it leaves the equatorial region. It is repelled by a force that depends upon r_g and gradient B, so that the component of momentum parallel to the magnetic line of force, p cos α, decreases and becomes zero ($\alpha = 90^o$) at the mirror point. The particle then spirals back to regions of lower magnetic flux density. In the absence of an electric field, the magnitude of the momentum, $|\,p\,|$, is constant.

If the spatial and temporal variation of the magnetic field is not too rapid, so that $r_g\,|\,\text{grad B}\,| \ll B$ and $\tau_1 dB/dt \ll B$, the path can be considered a circular motion about a center that moves along the line of magnetic force perpendicular to the circle and located at its center; this center is the guiding center. The rotating charge generates a magnetic moment parallel to B and of magnitude $p^2c^2(\sin^2\alpha)/2E_TB$. The repelling force is the product of this magnetic moment and dB/ds, where ds is the element of length along the guiding center path. Under the conditions of slow variation for which the guiding center approximation is valid, the magnetic moment is constant; it is called the first adiabatic invariant. For a constant magnetic moment (constant magnetic flux through the area πr_g^2),

$$B_m = B/\sin^2\alpha \,, \tag{17-10}$$

where B is the magnetic field at a position where the pitch angle is α, and B_m is the field at the mirror point. B_m depends only on the initial conditions of the particle direction and the magnetic field; it is independent of particle charge, mass, and energy.

The longitudinal invariant, or second adiabatic invariant, is

$$J_a = \int_{s1}^{s2} (p \cos\alpha)\, ds \,, \tag{17-11}$$

where ds is the element of path length of the guiding center from one mirror point, s1, to its conjugate, s2. From Eq. (17-10) and (17-11)

$$I = J_a/p = \int_{s1}^{s2} [1 - (B/B_m)]^{1/2}\, ds \,. \tag{17-12}$$

I is the invariant used in establishing the magnetic shell parameter L (Sec. 17.2.1); if the guiding center approximation is valid and if $\tau_2 \left| dB/dt \right| \ll B$, I is conserved.

The bounce period, τ_2, is the time of travel from one mirror point to the other and back;

$$\tau_2 = 2 \int_{s2}^{s1} \frac{E_T\, ds}{c^2 p \cos\alpha} \,. \tag{17-13}$$

If changes in the magnetic field are small within one azimuthal drift period, then there exists a third adiabatic invariant called the flux invariant. Within the guiding-center approximation, the flux invariant is equal to the magnetic flux enclosed by the guiding-center trajectory during a single drift around the earth. For example, if the geomagnetic field is slowly compressed (or expanded) the particle will also move inward (or outward) in such a way that the magnetic flux enclosed by the guiding-center trajectory will remain constant.

17.2 TRAPPED RADIATION

For convenience of discussion and consistency with definitions in the literature, the trapped electrons and protons are classified according to their location as follows:

(a) The inner zone (also called the inner Van Allen belt) where large temporal variations of the magnetic field do not occur and particle lifetimes are relatively long; and

(b) The outer zone (also called the outer Van Allen belt) where significant temporal variations of the geomatnetic field can occur, particle lifetimes are relatively short, and solar produced particles may be trapped (at least temporarily). A different classification, according to location in the magnetosphere, is becoming increasingly important as trapped radiation is considered a part of magnetospheric phenomena. Figure 17-3 illustrates the regions of stable trapping, pseudo trapping, and no trapping in the magnetosphere. Most of the trapped radiation is contained in the region of stable trapping, but during disturbed geomagnetic conditions the pseudo trapping region may contain trapped particles which will be lost in the earth's atmosphere at high latitudes.

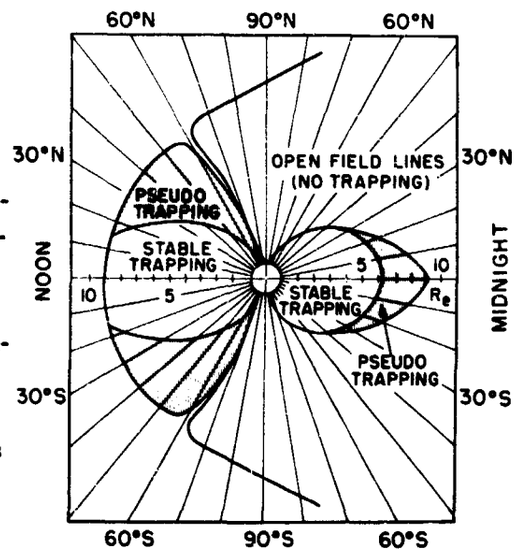

Figure 17-3. Cross Section of the Noon-Midnight Meridian Plane of a Model Magnetosphere, Showing Computed Limits of Stable Trapping and Pseudo Trapping Regions. Particles mirroring inside pseudo-trapping regions are unable to complete a 180° drift around the earth; those injected into the left-hand side will be lost into the tail whereas those injected into the right-hand side will abandon the magnetosphere on the day side through the boundary. (After Roederer, 1967).

The earliest measurements of trapped particles were obtained with relatively simple detectors that could not distinguish uniquely between various particle species and energies; hence the interpretation of these early data is somewhat ambiguous. Since late 1962, the instruments flown have been sufficiently sophisticated to enable unique interpretation of particle species and energy in all regions of the magnetosphere.

17.2.1 Spatial Parameters Characterizing Trapped Particles

In order to determine and describe the trapping regions, a two-parameter convention has evolved, which is based on the motion of the guiding center along a magnetic field line. In developing these parameters, the rapid particle-motion perpendicular to the field is ignored. If the slow drift around the earth is also ignored the guiding center moves along a single line of force between the mirror points. (The drift can be treated as a perturbation of this guiding-center motion.) Figure 17-2 shows the guiding-center path, the lines of magnetic force, and the reflection from one hemisphere to the other.

For any given azimuthal angle, two parameters suffice to describe this guiding-center motion. Two such parameters (by no means the only possible ones) are B_m, the scalar magnetic field at the point where the particle is reflected, and R_o, the maximum excursion of the guiding-center trajectory (i.e. the maximum distance of the magnetic field line from the center of the geomagnetic field.) Because B_m is an adiabatic invariant of the particle motion, it is a useful parameter with an obvious physical meaning. However, R_o is not an invariant. Due to the azimuthal asymmetry of the geomagnetic field, R_o for a given particle can vary as much as 10% as the particle drifts around the earth. The variation depends not only on the initial value of R_o and the azimuthal angle, but also on B_m.

The second adiabatic invariant, the longitudinal invariant I (Eq. 17-12), is available, but this does not have a clear physical or geometrical meaning. In a pure dipole field with moment M, R_o is determined by B_m and I; $R_o^3 B_m/M = f(I^3 B_m/M)$. In the geomagnetic field this relation does not hold. McIlwain [1961] replaced R_o by L and defined this new parameter by the relation

$$L^3 B_m/M = f(I^3 B_m/M), \qquad (17\text{-}14)$$

where the units of L are earth radii, (R_E), and $M = 0.311653$ gauss-R_E^3.

For particles traveling along a given field line, the L value depends only slightly on where the particles mirror. Because the geomagnetic field is nearly a dipole, $L \approx R_o$, and L has an approximate geometrical meaning. L can be calculated for any part of the geomagnetic field of interest; therefore, L and B_m are used extensively to describe the trapping regions.

It is implicit in the definition of L that the value of L at any given point in space is an adiabatic invariant of the motion of those particles which mirror at the given point [Stone, 1963]. All particles passing through the point do not in general have that particular value of L, but they do have L values within a few percent of it. The locus of all points with a given L value is called an L-shell. All particles with a particular L must mirror on the corresponding L-shell, but their motion may

otherwise deviate from the shell by distances equal to a few percent of L. From a practical standpoint, the accuracy of measurements has not progressed to a point where these deviations from an L-shell are significant, but ignoring them has led to confusion as to the significance of L. As more precise data become available, these details assume greater importance. Figure 17-4 shows contours of constant L and B at zero geographic longitude. Values of the magnitude of B at various altitudes and locations are given in Chapter 11; these values, however, should not be used for estimating fluxes below 1000-km altitude in the South Atlantic region.

Care must be exercised in comparing data on trapped particles when different models of the geomagnetic field were used to calculate the B-L coordinates. There are significant differences between various geomagnetic models, particularly at low altitudes over regional anomalies, that can result in apparent differences of trapped particle fluxes in B-L space; for a discussion of this problem, see Lindstrom and Heckman (1967).

The pitch angle at the geomagnetic equator is used sometimes as a more convenient parameter than B_m for interpreting results. In practice, the value of L is often calculated at the equator. The equatorial value does not correspond exactly to L at the mirror point, but is accurate to a few percent.

A coordinate system useful in obtaining an intuitive feeling for experimental results, as well as in the interpretation of data, effectively transforms the real geomagnetic field into a pure dipole representation. This is accomplished by substituting for B and L in the equations for a pure dipole field, the B and L of the real geomagnetic field. The coordinates are: R - the distance from the center of an effective dipole (not the centered dipole defined in Section 11.2.2.1); and λ - the equivalent geomagnetic latitude (similar to, but not identically the geomagnetic latitude used in Section 17.3).

The R, λ coordinates are obtained for any point in real space by calculating values of B and L for the main geomagnetic field, and substituting these values in the following equations:

$$R^6 + (3M^2/LB^2)\,R - 4M^2/B^2 = 0\,, \tag{17-15}$$

and

$$\cos^2\lambda = R/L\,, \tag{17-16}$$

where R and L are in earth radii and M is 0.311653 gauss-R_E^3. Equation (17-15) must be solved numerically, but when R and λ are specified, L is obtained directly from Eq. (17-16), and B from

$$B = M\,(4 - 3\cos^2\lambda)^{1/2}/R^3\,. \tag{17-17}$$

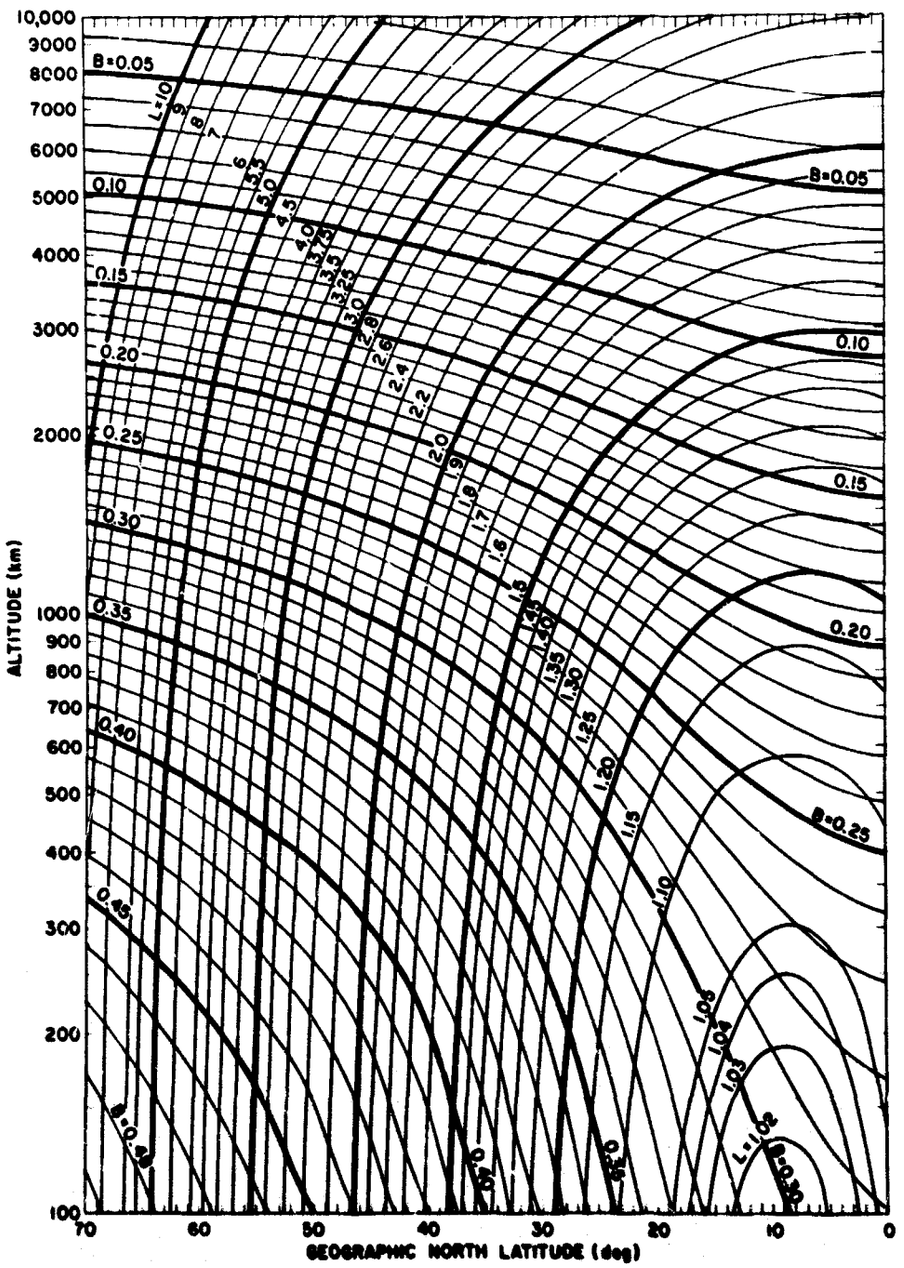

Figure 17-4 (a). Lines of Constant L (Earth Radii) and B (gauss) at Zero Geographic Longitude as a Function of Geographic Latitude and Altitude. [From Aerospace Corp. Rept. No. TDR 169 (3510-41), TR-4 Contract AF04 (695)-169]

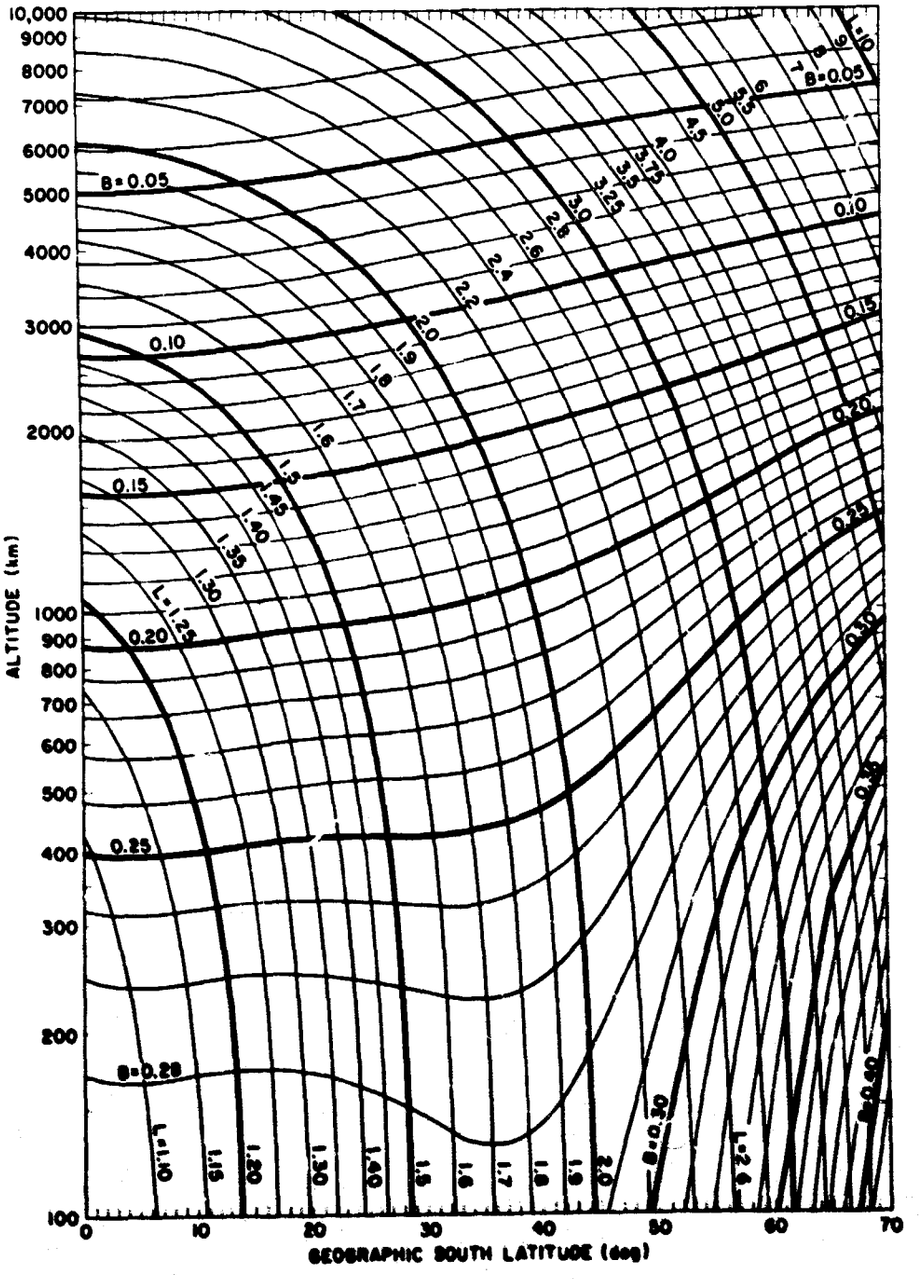

Figure 17-4 (b). Lines of Constant L (Earth Radii) and B (gauss) at Zero Geographic Longitude as a Function of Geographic Latitude and Altitude. [From Aerospace Corp. Rept. No. TDR 169 (3510-41), TR-4 Contract AF04 (695)-169]

Figure 17-5 shows the relation between parameters B_m and L and the coordinates R and λ. Essentially, these coordinates distort the geographic coordinates so that the earth becomes irregularly shaped, and the surface R = 1 in this coordinate system (referred to as the invariant earth) is not the earth's geoid. The actual earth's surface, the invariant surface, and a 1000-km polar orbit for 0° longitude in the R, λ system are included in Figure 17-14 for comparison.

17.2.2 Natural Injection and Loss of Particles

The mechanism by which protons and electrons are injected into the trapping region is not yet established. The hypothesis of a neutron-albedo source explains the presence of some of the trapped high-energy protons. High-energy neutrons are created in the upper atmosphere by cosmic rays, and some of the neutrons generated at the top of the atmosphere will be reflected back into space; these reflected neutrons are called the neutron albedo. A free neutron has a mean lifetime of about 12 minutes; it decays into a proton with almost the energy of the neutron, an electron with any energy up to 725 keV, and an antineutrino. If the neutron decays in the trapping region of the magnetosphere, the high energy proton (and the electron) can be trapped. This neutron-albedo source, however, is small and inadequate to supply the observed particle intensities (see Fig. 17-20). A possible source of trapped particles is solar corpuscular radiation that diffuses across magnetic field lines and is then accelerated. Lack of sufficiently precise observations at present has prevented the checking of several theoretical models proposed for this type of source.

Two important mechanisms by which high-energy trapped protons escape are interactions with the atmosphere and the failure of one or more of the adiabatic invariants. Atmospheric interaction losses generally occur in the region in which a particle mirrors. Collision with atmospheric particles decreases the trapped particle's energy by ionization loss. Small-angle scattering lowers the mirror point of any particle that is at or very near its mirror point. Catastrophic loss is a collision in which the trapped particle scatters directly into the atmosphere or loses most of its energy. Loss in the outer zone appears to be caused by failure of the trapping mechanism. This failure can result from the deviation of the geomagnetic field from a pure dipole, or from geomagnetic disturbances due to solar effects (Sec. 11.4.2). The breakdown of the trapping mechanism is presumed to limit the energy of a proton that can be trapped for long periods at high altitudes. Figure 17-6 shows the relation between maximum proton energy and the magnetic shell parameter as obtained from experimental data and as calculated by considering breakdown of the trapping mechanism.

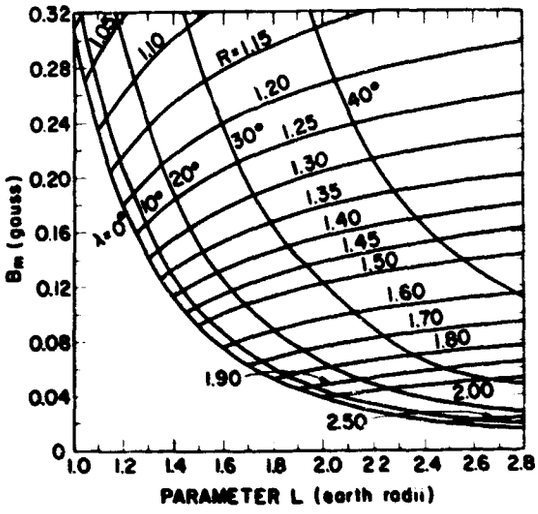

Figure 17-5. Transformation of Polar Coordinates R (Earth Radii) and λ (Degree) to Parameters B_m and L. (From McIlwain, 1961)

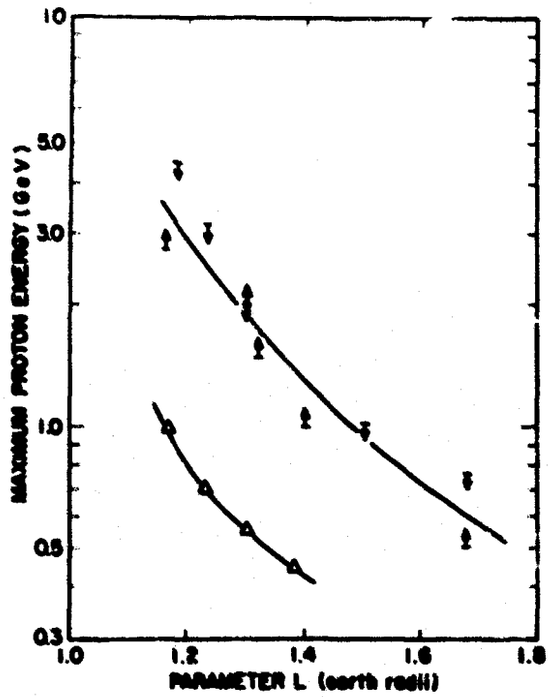

Figure 17-6. Maximum Proton Energy as a Function of the Magnetic Shell Parameter, Calculated from Breakdown of the Trapping Mechanism (upper curve) and from Explorer XI Observations (lower curve). (From Carmire, 1963)

In the outer zone the loss processes of low energy protons and electrons are complex. During observations, the measurement position varies with time in such a way that it is difficult to separate time variations from spatial variations. Nevertheless, adiabatic and non-adiabatic accelerations, diffusion, and pitch-angle scattering have been identified as processes which cause time variations in the outer region.

17.2.3 Effects of Nuclear Weapons Tests

The detonation of nuclear weapons at high altitude injects electrons into the trapping region and also causes a re-distribution of the trapped particles that were present in the natural environment. The largest perturbations observed were produced by the megaton weapons tested in 1962.

Table 17-1 gives some of the important parameters associated with some of these nuclear tests. The apparent mean lifetime (the time to decay to 1/e of the initial intensity) of the injected electrons differs radically from test to test. The Starfish burst (USA test on 9 July 1962) injected electrons with a long mean lifetime; these electrons were injected into a region of stable trapping ($L \approx 1.2$), and some were injected in equatorial regions at pitch angles near 90°. Electrons from USSR tests had relatively short lifetimes (they were not detectable after 6 months); these tests injected electrons at higher latitude and correspondingly larger L values. The number and spatial distribution of the naturally trapped electrons was not well known prior to the nuclear tests, hence it is difficult to firmly establish what fraction of the electrons subsequently observed were actually injected by the weapons tests.

It is assumed that proton fluxes measured after nuclear weapons tests are entirely natural, because no source of high-energy protons is expected from a thermonuclear detonation. However, the spatial distribution of high-energy trapped protons was affected; the magnitude of this redistribution is as yet unknown. Measurements by Filz and Loleman (1965) showed a definite increase in 55-MeV proton flux at low altitudes following Starfish. These observations were consistent with a pitch-angle redistribution of 3.5 degrees for 55-MeV protons in the inner zone. The larger increases occurred at the lower altitudes. This redistribution could have been caused by a magnetic disturbance from Starfish, as sufficient energy was available, but the actual mechanism is not understood. Other strange features are present in the measurements made after Starfish. The secondary peak of high-energy protons at the equator (see Figs. 17-10 and 17-14) is disappearing, but it will be necessary to make careful measurements for many years to separate the effects due to nuclear weapons tests from the effects due to geomagnetic storms and solar-cycle variations.

Table 17-1. Electrons Injected into Trapping Zone by High-Altitude Nuclear Tests, 1958-1962. (From Van Allen, 1966)

Designation	Date	Burst Altitude B(km)	Nominal Yield (TNT Equivalent)
Teak	1 Aug. 1958	~ 75	1C megaton
Orange	12 Aug. 1958	~ 45	10 megaton
Argus I	27 Aug. 1958	~200	1.4 kiloton
Argus II	30 Aug. 1958	~250	1.4 kiloton
Argus III	6 Sept. 1958	≳480	1.4 kiloton
Starfish	9 July 1962	~400	1.4 megaton
U.S.S.R. I	22 Oct. 1962	?	Submegaton
U.S.S.R. II	28 Oct. 1962	?	Submegaton
U.S.S.R. III	1 Nov. 1962	?	Megaton

Designation	Electron Flux* (no. $cm^{-2}s^{-1}$)	L-value of Burst	Apparent Mean Lifetime
Teak	10^3	1.1	Few days
Orange	10^3	1.1	Few days
Argus I	10^5	1.7	3 weeks
Argus II	10^5	2.1	3 weeks
Argus III	10^6	2.0	1 month
Starfish	10^9	1.12	1.5 years
U.S.S.R. I	10^7	1.9	1 month
U.S.S.R. II	10^7	2.0	1 month
U.S.S.R. III	10^7	1.8	1 month

*Maximum omnidirectional intensity at time of injection.

The Starfish electrons injected at high altitude and low L-value decayed as predicted from a diffusion theory developed by Walt (1966). Figure 17-7 shows the theoretical prediction and experimental data. At high values of B (low altitudes) the agreement is poor. This is because the measurements include the increased proton flux caused by Starfish. (The Geiger counter used to obtain the counting rates did not distinguish electrons from protons.) Figure 17-8 shows a comparison between experimental and calculated decay times of artificially injected electrons. Figure 17-9 shows the increase in electrons of energy greater than 1 MeV injected by the USSR tests in 1962. For further details, see West (1966) and Katz et al (1964).

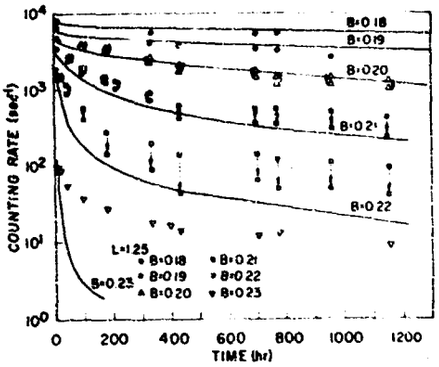

Figure 17-7. Predicted values (solid curve) for Decay of Trapped Electrons Injected by the Starfish Burst Compared with Observed Counting Rates; the Lower Value of a Set of Experimental Points is the Counting Rate Corrected for the Enhanced Proton Background. (From Walt and Newkirk, 1966)

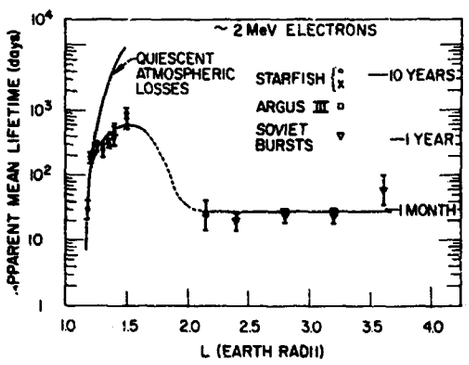

Figure 17-8. Apparent Mean Lifetime (τ) of Trapped Electrons; Decay was Assumed to be of the Form exp(-time/τ). (After Van Allen, 1966)

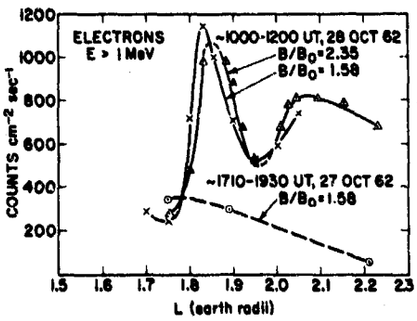

Figure 17-9. Change in Omnidirectional Flux of Electrons of Energy > 1 MeV Observed Before and After USSR Nuclear Tests in October 1962; B_0 is the Magnitude of the Magnetic Field at the Equatorial Crossing Point of the Particles

17.2.4 Trapped Protons

Protons with energies from thermal to about one GeV can be trapped in the earth's magnetic field. In general, the maximum energy of a proton trapped in a specific region of the magnetosphere is a function of the minimum field strength encountered along the particle's trajectory; the greater the value of the minimum field encountered, the greater the maximum energy of the protons. Consequently, the highest energy trapped-protons occur near the earth and are a principal component of the inner zone. In the outer zone the protons have lower energies because the L-shells on which they travel may extend to many earth radii, and the minimum value of the geomagnetic field strength is correspondingly small. The peak flux of the high energy protons is nearer the earth's atmosphere, while peaks for lower energies are progressively farther out. Figures 17-10 and 17-11 illustrate this variation outward along the equator.

For protons with energies above 10 MeV, the flux is relatively stable with time. Good model environments have been compiled by Vette (1966), which are adequate for most purposes. These proton models, however, do not describe the temporal variations and are not completely accurate at low altitudes.

The processes affecting the behavior of trapped protons are the same as those affecting the trapped electrons (Sec. 17.2.5). In the inner zone (excepting the lower edge where particle lifetime is controlled by the atmospheric density), proton fluxes tend to be stable in time and fairly insensitive to magnetic activity. In the outer zone beyond L=2, decreases in the proton flux have been associated with magnetic storms. McIlwain (1965) describes a sharp decrease in proton flux which occurred in less than a day. This decrease was energy dependent on a given L-shell, but the mechanism for this type of variation is not yet understood.

Figure 17-12 gives proton energy spectra measured at various L-shells. Figure 17-13 shows similar spectra for locally mirroring protons at the magnetic equator. These data indicate there is no typical energy spectrum; the form of the spectrum varies drastically with location. Figures 17-10 and 17-14 show the secondary peak in high-energy proton fluxes; it is not known at this time whether this secondary peak is a natural feature or a perturbation resulting from high altitude nuclear weapons tests. Detailed comparison of counting rates from Relay 1 shows that the softest spectrum occurs at L=1.9 a[illegible] the spectra become harder toward higher L values (Fillius and McIlwain, 1964).

Figure 17-15 gives the distribution of high-energy protons (60 to 120 MeV) in geographic longitude and latitude over the South Atlantic at about 670-km altitude. Figure 17-16 shows the energy spectrum of trapped protons at low altitude measured before and after the Starfish nuclear test. The agreement indicates that the shape of the energy spectrum did not change drastically.

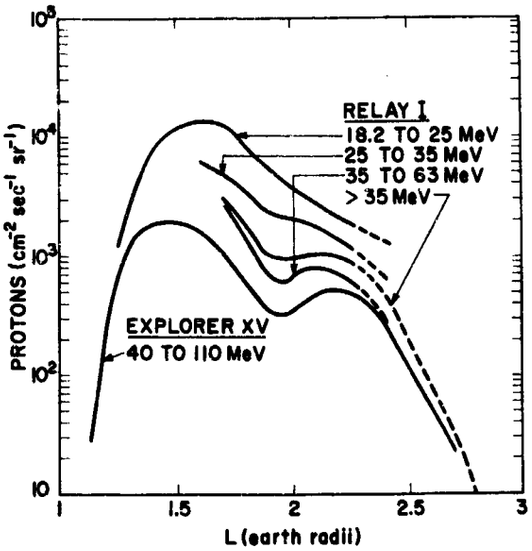

Figure 17-10. Directional Intensities of Protons Mirroring at the Magnetic Equator; Observations from Relay I (Dec. 1962-March 1963) Compared to Explorer XV (Nov. 1962-Feb. 1963). (After Fillius and McIlwain, 1964)

Figure 17-11. Directional Intensities of Protons with Equatorial Pitch Angle 60°. (After Davis and Williamson, 1966)

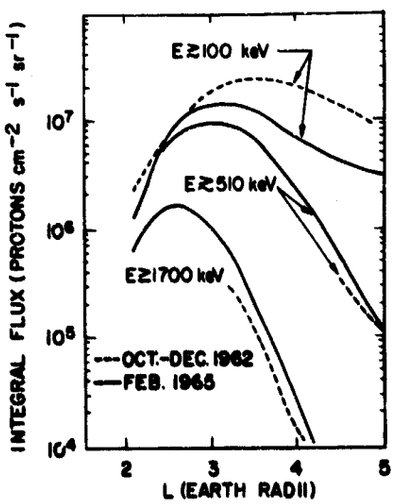

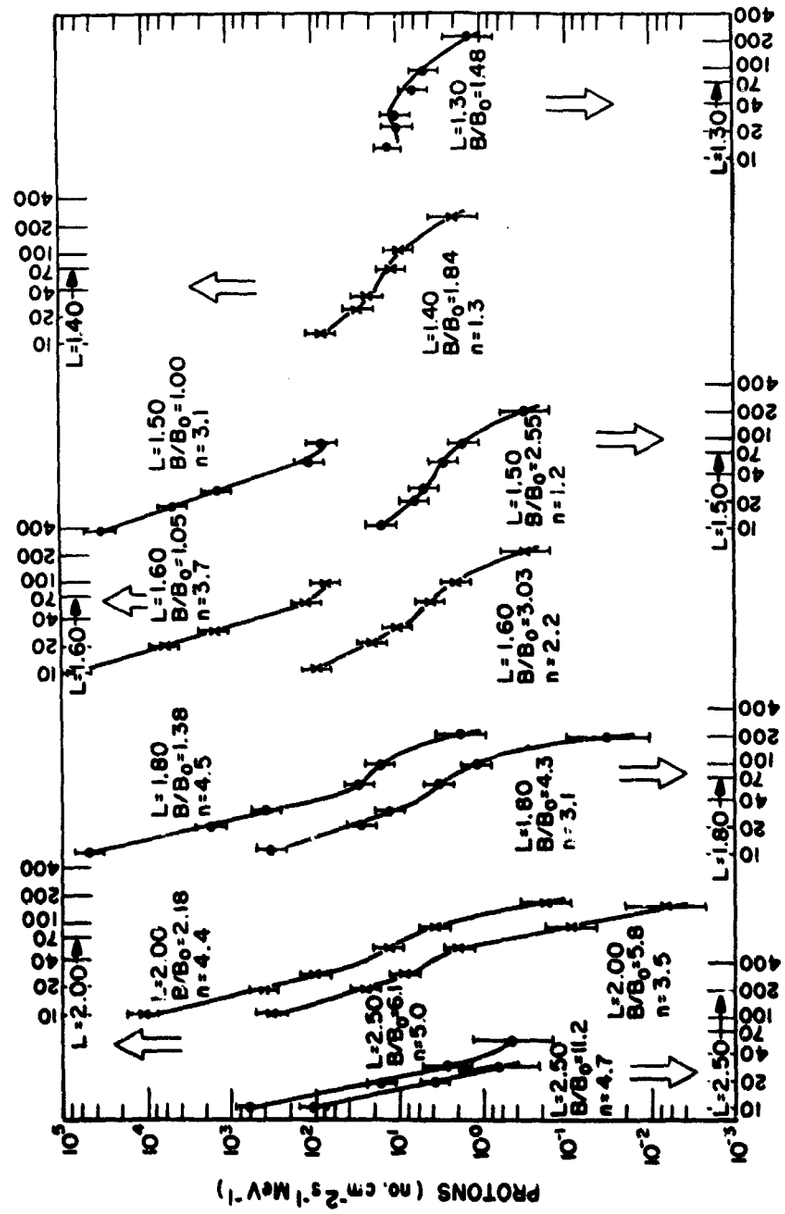

Figure 17-12. Differential Omnidirectional Proton Spectra as Functions of the Magnetic Shell Parameter (L) and the Ratio (B/B_0) of the Local Value of the Magnetic Field (B) to its Value at the Magnetic Equator (B_0) on the Same L-Shell. The solid curve through the data points at L = 1.30 is the spectrum of protons at $L \simeq 1.30$, $B/B_0 \simeq 1.41$ measured in 1960. The exponent n is obtained by fitting the spectrum in the 10 to 30 MeV region by a power law of the form E^{-n}. (After Freden et al., 1965)

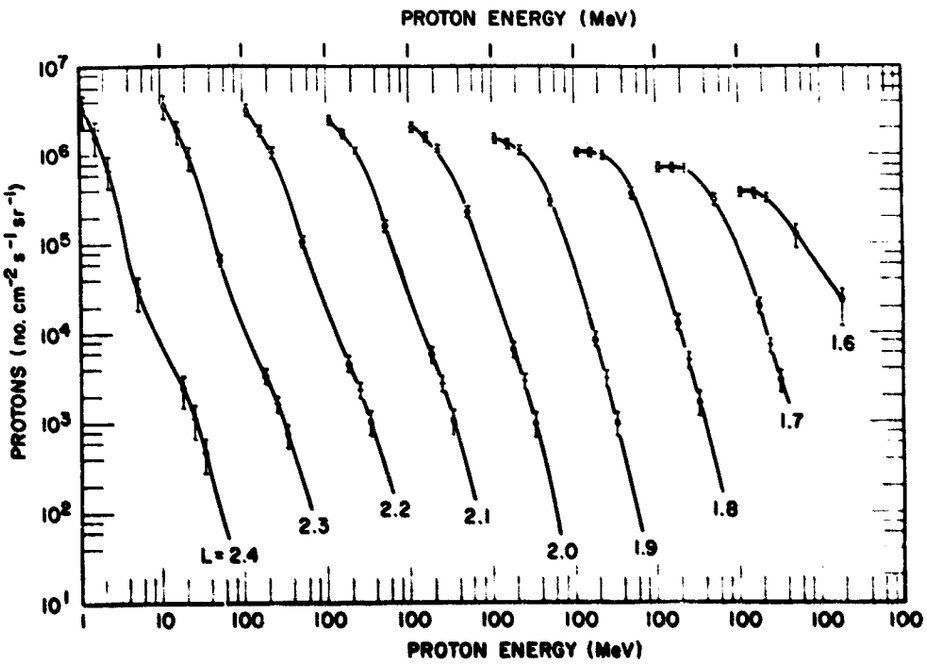

Figure 17-13. Integral Energy Spectra for Protons with Pitch Angles of 90° at the Magnetic Equator. Each Spectrum Extends from 1 to 60 MeV, and Values for the Logarithmic Energy Scale must be Shifted Accordingly. (From Fillius and McIlwain, 1964)

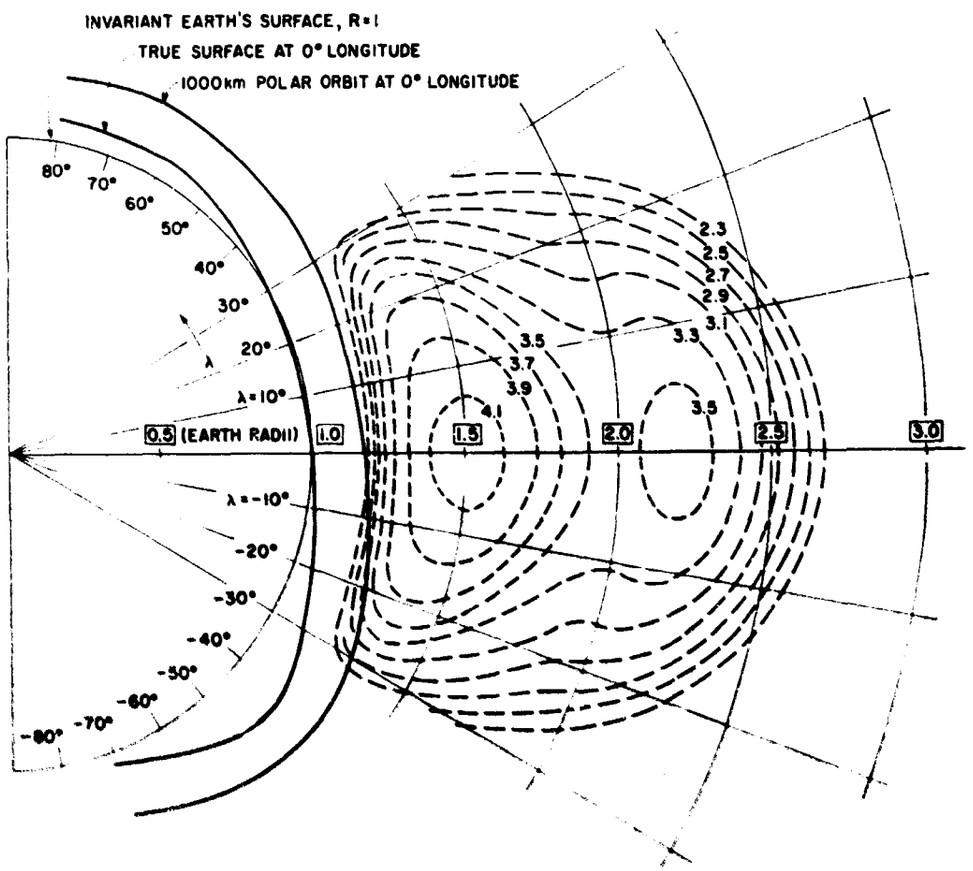

Figure 17-14. Isointensity Contours for 40 to 110 MeV Protons (Explorer XV Observations, Nov. 1962-Feb. 1963), Plotted in Polar Coordinates R and λ; Numbers Given on Contours are Units of $\text{Log}_{10}(1.4\ J_0)$, where J_0 is the Omnidirectional Flux (Protons $\text{cm}^{-2}\text{s}^{-1}$). The secondary peak at L ~ 2.2 was found to be a transitory feature; it may be an effect of the 1962 nuclear weapons. (After McIlwain, 1963)

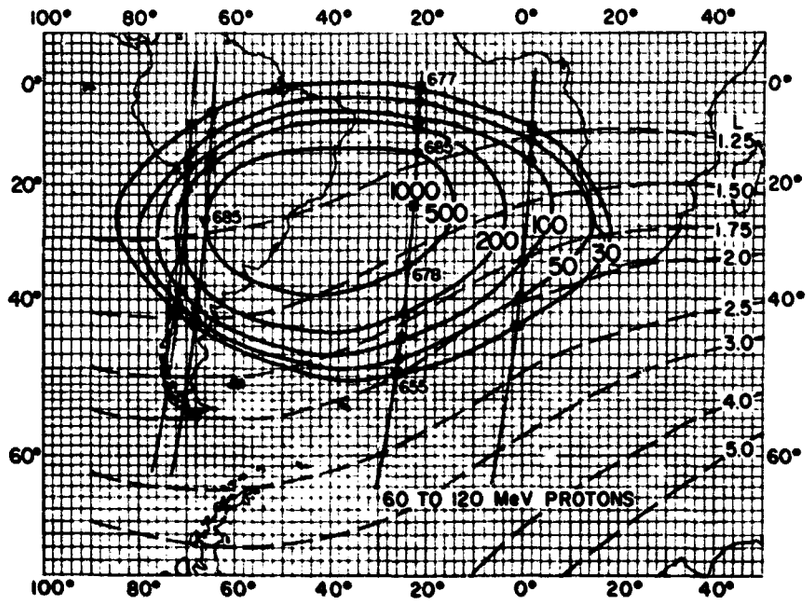

Figure 17-15. Isointensity contours for Protons Trapped Over the South Atlantic at Altitude 670 ± 15 km. Fluxes given on contours are protons $cm^{-2}s^{-1}$; the smaller numbers are typical altitudes (km) at which measurements were made. Dashed lines are contours of constant L-value. (From Freden and Paulikas, 1964)

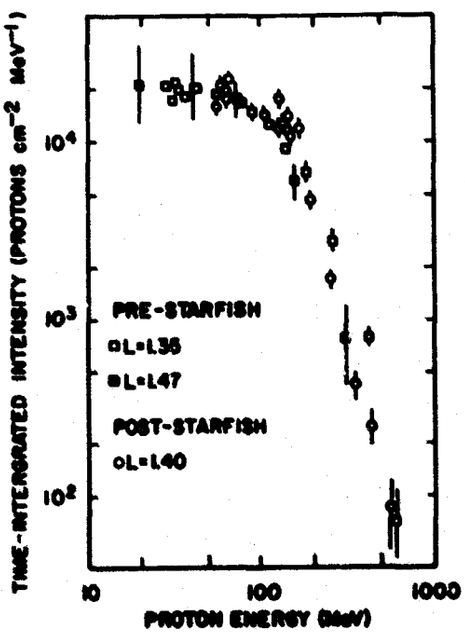

Figure 17-16. Omnidirectional Energy Spectrum of Protons at 408-km Altitude Over the South Atlantic. Circles indicate data taken several months after Starfish, at L = 1.4 and B = 0.218 gauss. Squares indicate data prior to Starfish; filled squares for L = 1.47, open squares for L = 1.35. (From Heckman and Nakano, 1965)

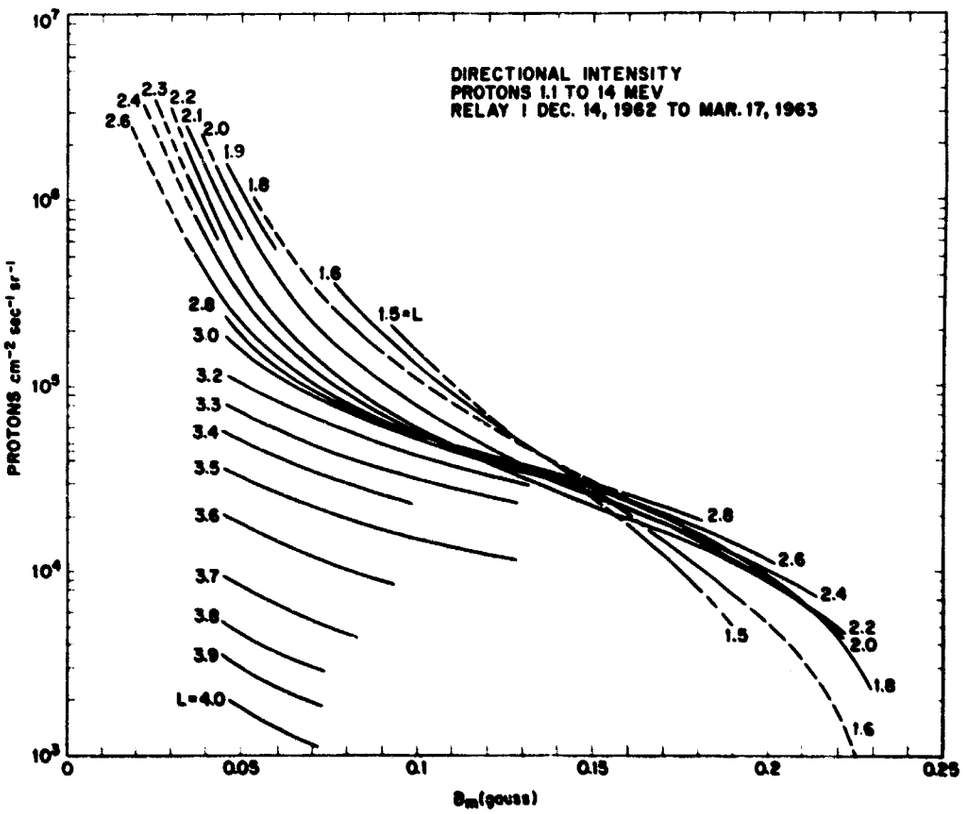

Figure 17-17. Intensities of Locally Mirroring Protons in Various Magnetic Shells; Dashed Lines are Extrapolated or Interpolated. The magnetic equator is the minimum value of B_m for the particular L value except for L = 2.1 and 1.9 earth radii; these are not extrapolated to their minimum B_m. (From Fillius and McIlwain, 1964)

Figure 17-17 shows observations of the directional intensity of low-energy protons; the flux of locally mirroring protons is plotted as a function of the magnetic field at the mirror point for various magnetic shells. The intensity and the spatial distribution of these low-energy protons are not in accord with predictions based on the hypothesis of a neutron-albedo source.

The most extensive time histories of energetic protons in the lower edge of the inner zone are available from recoverable-satellite nuclear-emulsion measurements (Filz and Holeman, 1965; Filz, 1968). Figure 17-18 shows the 55-MeV flux measurements from 1961 to 1967 normalized to altitudes of 275, 350 and 400 km. The solid curves following July 1962 show the theoretical decay

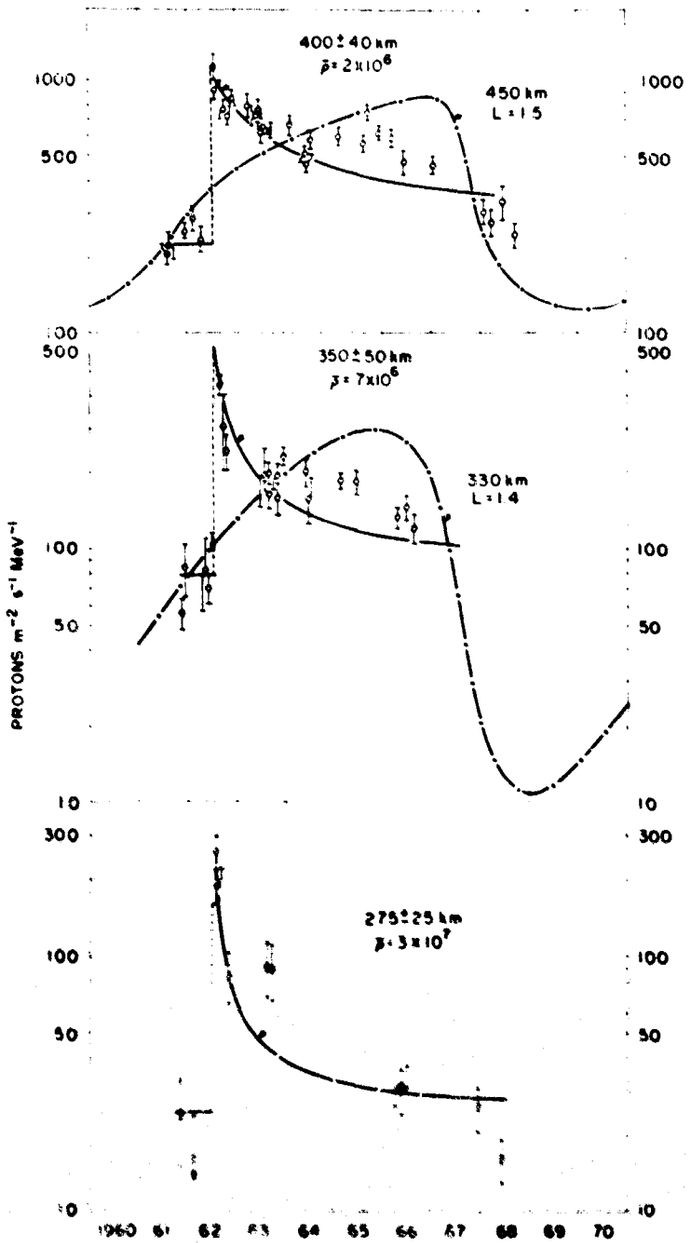

Figure 17-18. Time Histories of 55-Mev Proton Fluxes at Various Altitudes. The solid curves represent the theoretical decay expected following Starfish (July 1962); $\bar{\rho}$ (atomic electrons per cubic centimeter) is the measure of average atmospheric density used to compute the theoretical decay. The dashed lines show the increase caused by Starfish. The dash-dot curves show the time behavior predicted on the basis of solar-cycle changes in atmospheric density and a neutron-albedo source

based on ionization loss in the average atmosphere (Cornwall et al, 1965). $\bar{\rho}$ is the average number of atomic electrons per cubic centimeter of atmosphere at the given altitudes, and is used as a measure of the mean atmospheric density encountered by trapped protons. The predicted time variation of proton fluxes due to solar-cycle changes in atmospheric density (Blanchard and Hess, 1964) is shown at 330 and 450 km in Figure 17-18. Figure 17-19 gives the altitude distribution of 55-MeV protons observed prior to Starfish. Figure 17-20 compares these measurements with the distributions predicted by the neutron-albedo hypothesis of particle injection; the predicted values are multiplied by a factor of 50 to obtain the plotted curves. The measurements of 55-MeV protons are representative of high-energy protons in the inner radiation zone. The increase in proton flux following Starfish has prevented precise measurements of the natural variation with time of proton fluxes in the lower region during the period of observation.

The measurements do, however, lead to two important conclusions. First, the decay of protons after Starfish is consistent with that expected from energy loss by ionization in the upper atmosphere. Second, the decay levels off as expected, because at these altitudes the atmospheric density was decreasing as the 11-year sunspot cycle approached minimum in October 1964. When corrected for the Starfish residual, the 1965 fluxes are about twice the 1962 fluxes (Filz, 1967). This is reasonably consistent with the calculations of Blanchard and Hess (1964). Calculations of fluxes using the neutron-albedo hypothesis do not agree with the observations. As Figure 17-20 shows, the undisturbed fluxes measured in 1961-1962 are larger by a factor of fifty than those predicted by calculations of the neutron-albedo source strength.

17.2.5 Trapped Electrons

The temporal behavior and the spatial extent of trapped electrons with energies above 40 keV depend upon geomagnetic activity and upon solar activity that influences conditions in the magnetosphere. Geomagnetic activity results in (and can be the result of) significant changes in the flux and spectra of the trapped electrons. Figure 17-21 shows the correlation between the variation in geomagnetic activity (as denoted by the magnetic activity index K_p) and the variations in flux on different L-shells in the outer zone. Figure 17-22 illustrates the variation in spectra with geomagnetic activity. Because the spectra obtained in the outer region are highly variable, there is no typical electron spectrum. Sometimes the spectra depend upon the L-value, as expected for particles whose source is radial diffusion conserving the first two adiabatic invariants. At other times the spectra are independent of the L-value. The model electron environment developed by Vette et al (1966) is the best model available at this time; this model is for inner and outer zone electrons with energies greater than 0.5 MeV.

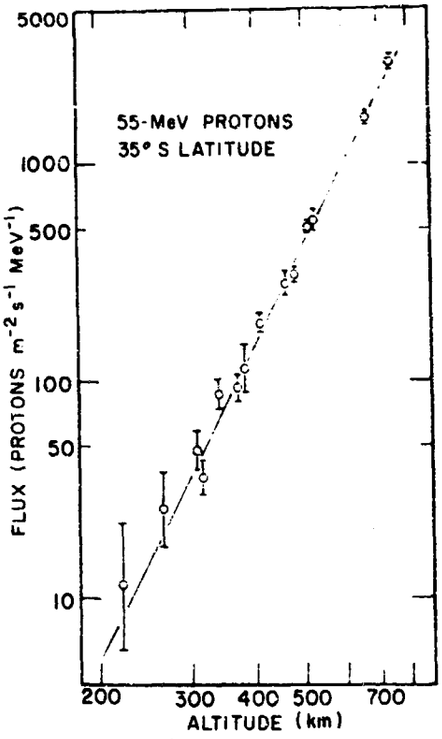

Figure 17-19. Altitude Distribution of 55-MeV Protons During the Period August 1961 to June 1962 in the Region of the South Atlantic at 35°S Latitude. The altitudes given are altitudes of the guiding center; the solid line is the weighted least-squares fit to the data. (From Filz and Holeman, 1965)

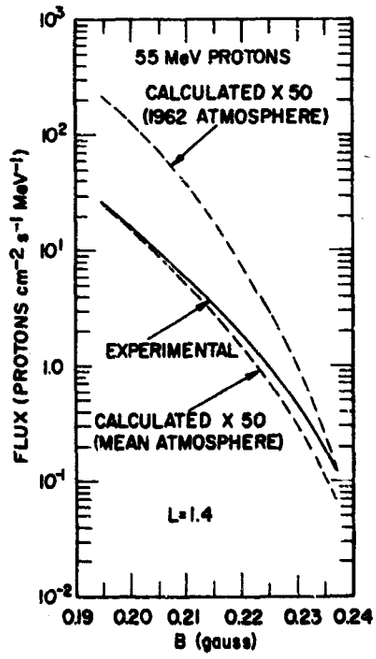

Figure 17-20. Omnidirectional Fluxes of 55-MeV Protons Determined by Experiment Compared with Those Predicted by Calculations of Neutron-Albedo Source Strengths; Calculated Values were Multiplied by 50 to Obtain the Dashed Curves. (After Dragt et al, 1966)

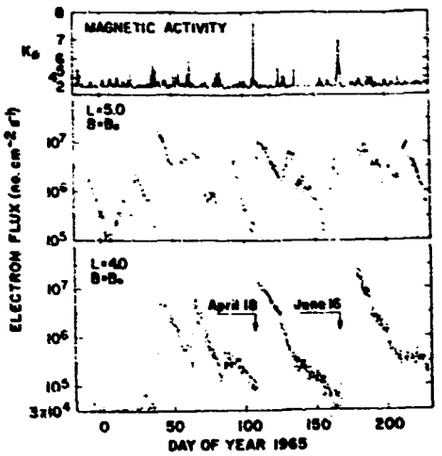

Figure 17-21. Decay of Electrons with Energies Greater than 0.5 MeV at the Geomagnetic Equator ($B = B_0$) in the Outer Zone (L Shells 4.0 Earth Radii and 5.0 Earth Radii) Compared with the Variation in Magnetic Activity Index, K_p. (After C. E. McIlwain, "Processes Acting upon Outer Zone Electrons: 1, Adiabatic Perturbations", Report USCD-SF-66-5, 1965)

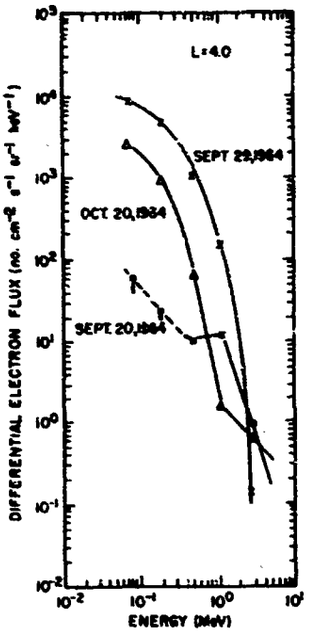

Figure 17-22. Spectra of Electrons Trapped in Outer Zone at L = 4.0 Earth Radii for a Geomagnetically Disturbed Day (29 Sept. 1964), a Somewhat Disturbed Day (20 Oct. 1964) and a Quiet Day (20 Sept. 1964); the Dashed Line indicates an Upper Limit to the flux. (From Pfitzer et al, 1966)

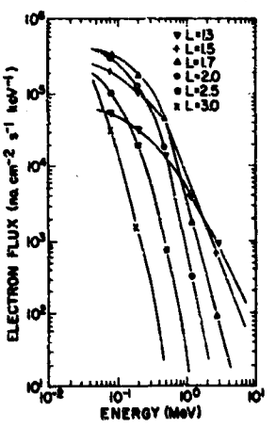

Figure 17-23. Typical Energy Spectra of Electrons in Various L Shells (1.3 to 3.0 Earth Radii); Flux Values Include Electrons Injected by the 1962 Nuclear Weapon Tests. (From Pfitzer et al, 1966)

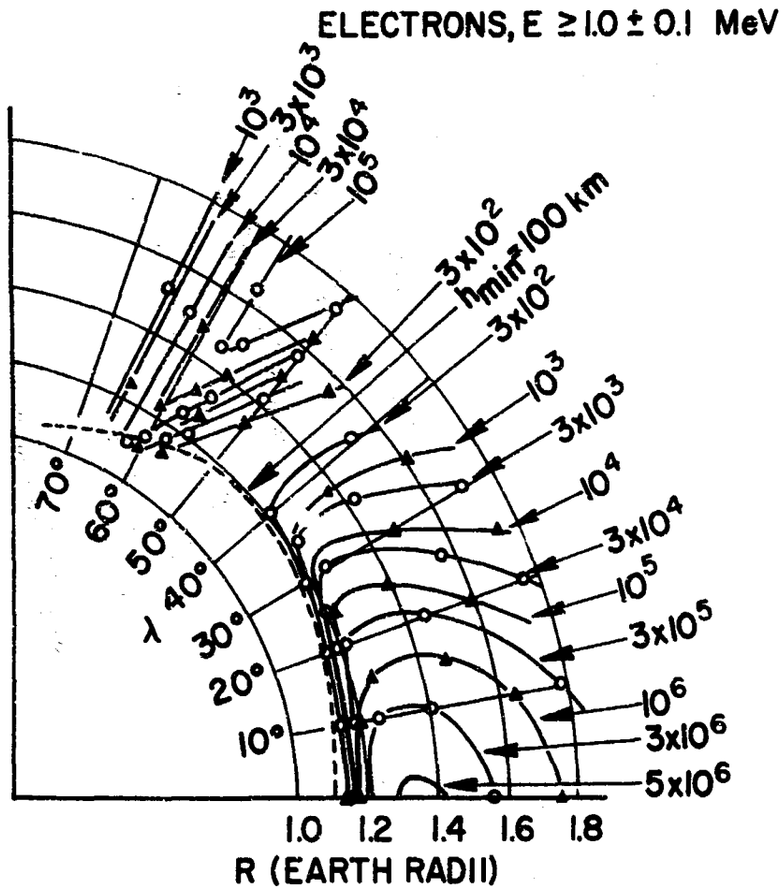

Figure 17-24. Contours of Constant Intensity of Inner Zone Electrons with Energies Greater than 1.0 MeV ± 0.1 MeV During July-August 1963; Flux Values Given are Electrons $cm^{-2}s^{-1}sr^{-1}$. (Data from Paolini and Theodoridis, 1967)

The inner zone is much more stable than the outer zone, hence typical energy spectra and intensity maps are available. Figure 17-23 gives the omnidirectional differential spectra for electrons during November 1962 at various L-values in the inner zone. Because these measurements include electrons injected by the 1962 nuclear weapons tests and fission-produced electrons have a characteristic hard spectrum, the spectra in Figure 17-23 should be considered an upper limit. Figure 17-24 is a typical contour map for electrons with energies greater than 1 MeV obtained during August 1963.

The processes responsible for time variations in electrons trapped in the outer region may be grouped phenomenologically into four categories: (1) rapid

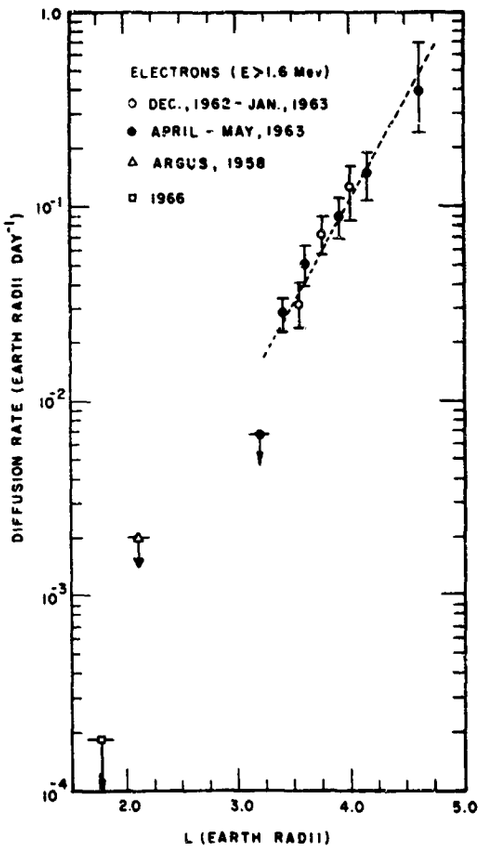

Figure 17-25. Apparent Rate of Inward Radial Diffusion of Electrons with Energies Greater than 1.6 MeV; the Straight Line has been Drawn Through the Data Points. (After Frank, 1966 and Brown, 1966).

non-adiabatic accelerations resulting in the gain (or loss) of particle number or of particle energy; (2) adiabatic accelerations with a gain (or loss) of particle energy; (3) non-adiabatic diffusion; and (4) persistent decay. At any particular time one process may dominate, although all processes can occur simultaneously.

Rapid non-adiabatic acceleration of electrons may be caused by magnetic and electric fields which depend on time and longitude; such fields can result from plasma instabilities (McIlwain, 1966; Chang, 1966; and Kennel and Petschek, 1966). When non-adiabatic acceleration occurs, there may be changes in the number and/or the energy of the electrons. The sharp increases in the omnidirectional fluxes shown in Figure 17-21 are probably due to a non-adiabatic acceleration.

The magnetic fields due to ring currents and currents on the boundary of the magnetosphere may result in adiabatic accelerations of outer-zone electrons. The changes in electron intensity caused by ring currents can be identified in the experimental data (McIlwain, 1966). The time variations of these magnetic fields result in betatron acceleration of electrons which are already trapped.

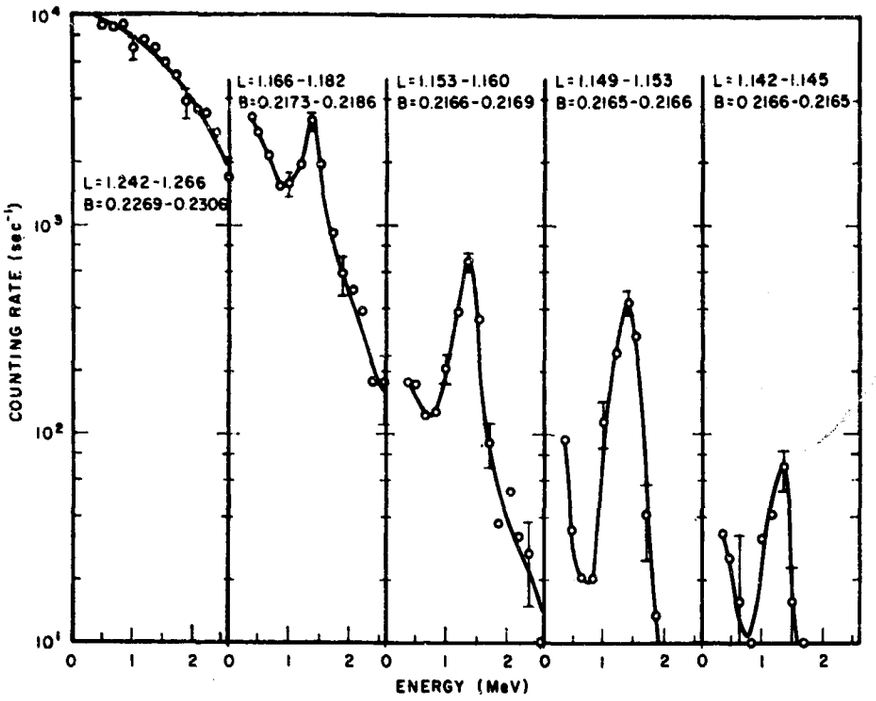

Figure 17-26. Electron Energy Spectra in the Lower Region of the Inner Belt Over the South Atlantic (61°W Longitude, 22° to 35° S Latitude) on 30 Oct. 1963 (1733 to 1738 hour Universal Time); Data Points are not Corrected for Detector Response. The fluxes shown here are the result of a selective redistribution and are higher than those observed on prior satellite passes in the same region. (From Imhof and Smith, 1966)

Diffusion of electrons across L-shells is the result of a breakdown of the third adiabatic invariant while the first two invariants are conserved (Dungey, 1965). Under these conditions, electrons gain energy as they diffuse radially inward; the diffusion rate will depend upon the L-value. Figure 17-25 shows the apparent rate of inward radial diffusion for electrons measured by Explorers IV, XIV, and XV. Diffusion across L-shells can also be caused by what is known as L-shell splitting and pitch-angle diffusion (Roederer, 1967). Because of the day-night asymmetry of the magnetosphere, particles on the same L-shell mirror at different points on the night side of the earth than on the day side. When particles undergo pitch-angle changes on the day side, they change both their mirror point and L-value. This type of diffusion does not significantly change the particle energy.

Electrons trapped in the outer zone undergo a persistent decay. Figure 17-21 shows examples of the decay on two different L-shells. This persistent decay of

the omnidirectional flux on the geomagnetic equator is approximately exponential in time, as the semi-log plot of Figure 17-21 demonstrates. If the dominant loss mechanism removes a fixed fraction of electrons per unit time, then the decay of the observed flux will be of the form exp (-time/τ); τ is observed to be of the order of two weeks. Non-adiabatic pitch-angle scattering into the loss cone by interactions with electromagnetic waves and the subsequent loss of particles in the atmosphere is consistent with this decay process.

The processes which modulate electrons trapped in the outer zone, influence the electrons trapped in the inner zone to a lesser extent. For example, selective redistribution of electrons has been observed at low altitudes; this may result from a combination of the above phenomena. Figure 17-26 illustrates the result of a selective redistribution on the electron energy spectra in the lower region of the inner zone. The enhanced fluxes shown in Figure 17-26 were probably caused by a redistribution of electrons in the inner zone. This redistribution was correlated quite strongly with magnetic activity.

The radial diffusion coefficient for inner belt electrons has been measured by observing artificially injected electrons (Brown, 1966). As Figure 17-25 shows, the diffusion coefficient is much smaller in the lower edge of the inner zone than is characteristic of the rest of the inner zone.

17.3 COSMIC RADIATION

Primary cosmic radiation is a small flux of high-energy particles of extraterrestrial origin. Galactic cosmic radiation is of galactic or extragalactic origin and is believed to exist throughout all space unoccupied by dense matter. The flux of galactic cosmic radiation is essentially isotropic with some minor deviations. The galactic cosmic-ray flux, as observed at the earth, is modulated by the interplanetary magnetic field, and is minimum at periods of maximum solar activity.

The primary cosmic radiation that reaches the earth is composed of galactic and, at times, solar particles. Within the magnetosphere these particles follow curved paths dictated by the magnetic field. The primary particles incident on the top of the atmosphere collide with nuclei in the atmosphere initiating a nuclear cascade of secondary cosmic-rays; the ratio of primary to secondary particles is a function of altitude.

17.3.1 Composition and Energy

The galactic cosmic-ray flux is 83% protons, 12% alpha particles, 1% nuclei of other elements (often called heavy primaries), 1% gamma rays and 3% electrons (about 1/10 of the electrons are positive). Antimatter has not yet been identified

in the primary flux; if it is present, its flux must be less than 0.01% (present experimental limit) of the primary flux. Figure 17-27 shows relative cosmic-ray abundances of primary cosmic-ray nuclei compared with universal abundances of the elements. The much greater proportion of lithium, beryllium, and boron present in the cosmic radiation is attributed to their production by fragmentation of heavier cosmic-ray particles colliding with the interstellar gas.

The background flux of primary protons and alpha particles impinging on the top of the atmosphere with energies greater than 500 MeV is about 0.2 proton $cm^{-2}s^{-1}sr^{-1}$ and 0.03 alpha particle $cm^{-2}s^{-1}sr^{-1}$ respectively. Figure 17-28 presents the best available rigidity spectra for protons, alpha particles and heavy nuclei of charge greater than 6 at solar minimum. Figure 17-29 gives the differential energy spectra for protons and alpha particles, also at solar minimum.

Accurate data for galactic electrons are not available at this time. Figure 17-30 summarizes the current state of knowledge; both experimental and theoretical data are combined to yield the best differential energy spectra available. Figure 17-31 gives the integral energy spectrum and shows the available experimental data points.

17.3.2 Geomagnetic Field Effects

The cosmic-ray particles that arrive at any point on the earth's surface have undergone deflection in the geomagnetic field; this has the effect of causing amplitude and time variations in the observed cosmic-ray flux. In order to relate variations observed on the ground to variations of the primary cosmic radiation in space, it is essential to make allowance for these deflections.

In studies of time variations of cosmic radiation, a knowledge of the dependence of the detector counting rate on the asymptotic direction (the direction from which the particle was traveling before being deflected by the geomagnetic field) is necessary. In such studies the concept of the asymptotic cone of acceptance is used. This may be defined as the solid angle containing those asymptotic directions of approach which make a significant contribution to the counting rate of the detector (or more simply, the acceptance solid angle in celestial coordinates). McCracken et al (1965) and Shea et al (1968a) list the geographic coordinates and the asymptotic directions of approach for most of the cosmic-ray stations around the earth.

Variations of the cosmic-ray intensity with latitude (and to a lesser extent with longitude) are due to differences of the geomagnetic cutoff rigidity at various locations on the earth. If the rigidity (see Eq. 17-8) of the primary nucleus is equal to or greater than the cutoff rigidity for a given location, the particle can penetrate the geomagnetic field and arrive at the specified location. The classic

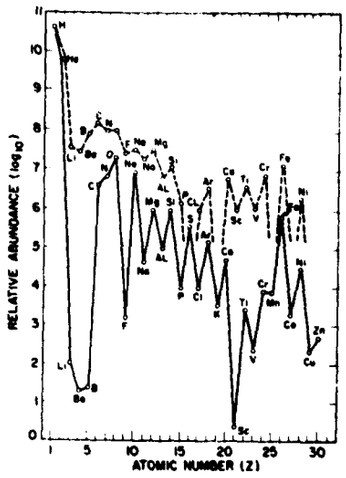

Figure 17-27. Relative Abundance of Nuclei in the Primary Galactic Cosmic Radiation (Dashed Line) Normalized to the Cosmic Abundance of Hydrogen, and Relative Cosmic Abundance of the Elements (Solid Line). (After C. J. Waddington, "Progress in Nuclear Physics," J.G. Wilson, ed., v. 8 Pergammon Press, N.Y., 1960)

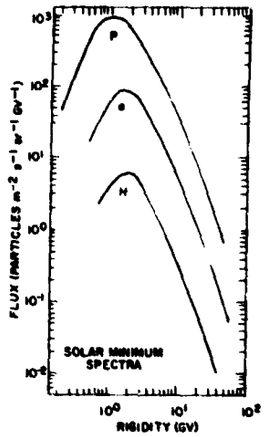

Figure 17-28. Rigidity Spectra of Galactic Cosmic Ray Particles near Solar-Cycle Minimum: P, Protons; α, alpha particles; H, Nuclei with Charge Greater than 6. (After Anand et al, 1968)

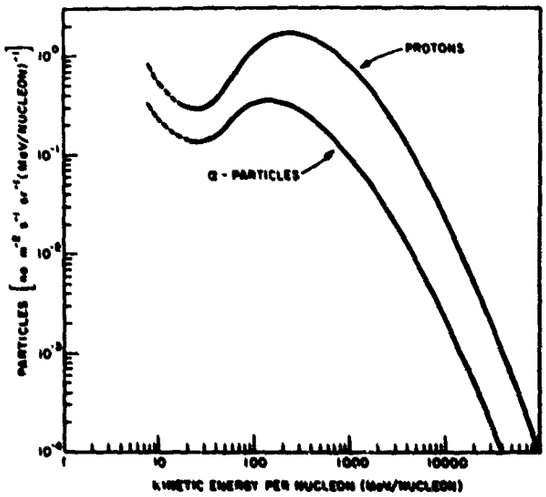

Figure 17-29. Differential Energy-per-nucleon Spectra of Galactic Cosmic Ray Protons and Alpha Particles Observed near the Time of Solar Minimum. (After Gloeckler and Jokipii, 1967)

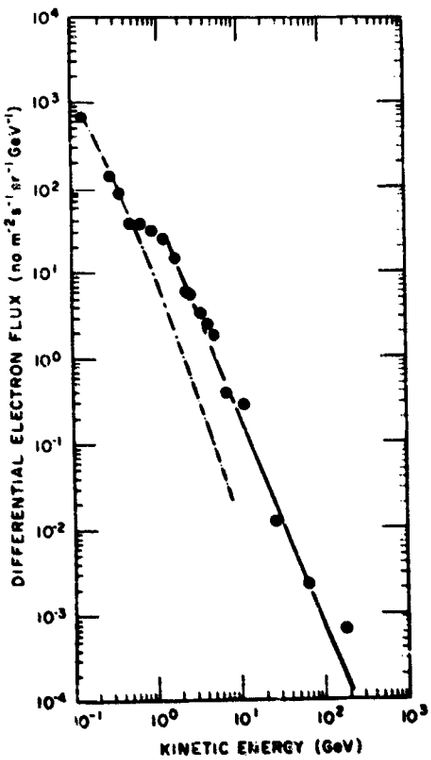

Figure 17-30. Differential Energy Spectrum of Primary Cosmic Ray Electrons. The solid line is a least-squares fit to the data for energies above 1.5 GeV. The dot-dash curve represents calculated equilibrium energy-spectra of electrons produced by cosmic-ray interactions in the Galaxy. (After L'Heureux, 1967)

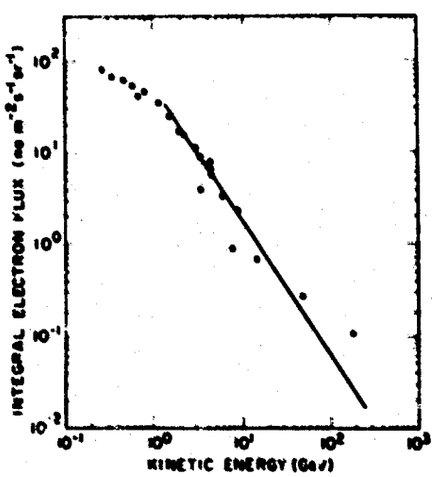

Figure 17-31. Integral Spectrum of Primary Electrons of Galactic Cosmic Rays; the Solid Line is a Least-Squares Fit to the Data for Energies Above 1.5 GeV. (After L'Heureux, 1967)

work of Stormer on the motions of particles in a dipole magnetic field results in the following equation for determining the cutoff rigidity, P_c:

$$P_c = Mc \cos^4\lambda / R_E^2 \left[1 + (1 - \sin\epsilon \sin\phi \cos^3\lambda)^{1/2}\right] \quad (17\text{-}18)$$

where M is the geomagnetic dipole moment (3.1165×10^{-5} T·R_E^3; 198.77 V·s·R_E^2·m^{-1}; 0.31165 gauss·R_E^3; 8.05×10^{25} gauss·cm^3), c is the speed of light, λ is the geomagnetic latitude, R_E is the earth's radius, ϵ is the zenith angle and ϕ is the azimuthal angle measured from the north. Equation 17-18 is valid in SI (MKSA) and EMU systems of units.

By common usage, the cutoff at a specific location is the minimum rigidity for which cosmic rays can arrive at the location from vertical incidence (zenith angle zero). For particles arriving vertically, Eq. 17-18 reduced to

$$P_c = Mc \cos^4\lambda / 4 R_E^2 \quad (17\text{-}19)$$

or,

$$P_c = 14.9 \cos^4\lambda \text{ [GV]} . \quad (17\text{-}20)$$

The approximation does not allow for deviations of the earth's magnetic field from the dipole model due to the displacement of the geomagnetic center from the geocenter, for deviations due to magnetic anomalies, or for the actual magnetospheric configuration. In a dipole field $\cos^2\lambda = R_E/L$, so in terms of the McIlwain coordinate L, Eq. (17-20) becomes

$$P_c = 14.9 L^{-2} \text{ [GV]} . \quad (17\text{-}21)$$

No analytic equations exist for calculation of cutoff rigidities in the actual geomagnetic field, although many approximations have been tried. In practice, a unique threshold does not exist in mid-latitude regions where there are alternating bands of allowed and forbidden rigidities near the cutoff rigidity (penumbral effect). The method currently accepted as most accurate is a calculation of the trajectories of cosmic-rays through a spherical harmonic expansion of the earth's field (Sec. 11.2.2.1) in order to determine if a given particle rigidity is allowed or forbidden at a specified location. Table 17-2 lists by geographic longitude and latitude the best available vertical cutoff rigidities determined by the trajectory tracing method (Shea et al, 1968b).

Table 17-2. Vertical Cutoff Rigidities (GV)

Geographic latitude	Geographic longitude (E)											
	0	15	30	45	60	75	90	105	120	135	150	165
85	0.01	0.02	0.02	0.03	0.03	0.04	0.04	0.04	0.04	0.04	0.03	0.03
80	0.03	0.05	0.07	0.09	0.10	0.12	0.13	0.14	0.12	0.13	0.12	0.09
75	0.12	0.15	0.21	0.23	0.26	0.28	0.28	0.29	0.31	0.29	0.29	0.27
70	0.29	0.37	0.44	0.49	0.52	0.56	0.56	0.60	0.64	0.64	0.62	0.61
65	0.60	0.73	0.88	0.93	1.00	1.01	1.04	1.10	1.17	1.21	1.22	1.19
60	1.14	1.37	1.50	1.65	1.69	1.74	1.81	1.89	2.01	2.06	2.16	2.10
55	2.02	2.24	2.54	2.61	2.74	2.78	2.92	2.99	3.14	3.41	3.40	3.24
50	3.06	3.52	3.88	4.05	4.15	4.28	4.39	4.58	4.76	4.98	4.95	4.71
45	4.71	5.18	5.42	5.62	5.76	5.98	6.18	6.34	6.64	6.94	6.95	6.47
40	6.64	7.37	7.57	7.81	8.23	8.75	9.16	9.39	9.68	9.94	9.80	9.03
35	9.49	9.86	9.95	10.61	11.10	11.65	11.66	11.84	12.00	12.07	11.59	10.76
30	11.24	11.76	12.13	12.64	13.31	14.07	14.44	14.51	14.35	14.04	13.55	12.88
25	12.99	13.59	14.06	14.46	14.99	15.56	15.91	15.88	15.58	15.12	14.55	13.92
20	14.01	14.56	14.99	15.44	16.01	16.59	16.92	16.84	16.45	15.91	15.31	14.72
15	14.51	15.05	15.52	16.01	16.61	17.20	17.52	17.42	17.00	16.44	15.87	15.34
10	14.66	15.16	15.65	16.18	16.81	17.40	17.71	17.63	17.24	16.72	16.21	15.77
5	14.49	14.92	15.41	15.98	16.62	17.20	17.52	17.50	17.19	16.74	16.32	15.98
0	14.03	14.37	14.84	15.43	16.08	16.63	16.95	17.01	16.82	16.49	16.17	15.95
−5	13.34	13.55	13.98	14.57	15.20	15.70	16.01	16.16	16.12	15.92	15.73	15.64
−10	12.45	12.52	12.89	13.46	14.02	14.43	14.71	14.95	15.04	14.99	14.93	14.98
−15	11.09	11.16	11.53	12.02	12.39	12.74	12.99	13.26	13.44	13.58	13.68	13.91
−20	9.55	9.38	9.70	10.00	10.28	10.30	10.36	10.60	10.96	10.77	10.94	12.02
−25	8.07	7.76	7.90	8.14	8.07	7.60	7.11	7.19	7.60	7.91	8.64	9.66
−30	6.85	6.22	6.10	5.91	5.68	5.37	5.12	5.08	5.20	5.54	5.98	6.73
−35	5.66	4.83	4.59	4.41	4.24	3.91	3.36	3.28	3.44	3.72	4.26	4.89
−40	4.58	3.92	3.59	3.32	2.95	2.63	2.18	2.02	2.09	2.28	2.70	3.31
−45	3.74	3.13	2.70	2.38	2.06	1.60	1.35	1.17	1.14	1.27	1.55	2.05
−50	3.15	2.44	2.07	1.74	1.37	1.04	0.76	0.60	0.55	0.64	0.83	1.15
−55	2.47	1.89	1.53	1.19	0.88	0.59	0.39	0.28	0.23	0.27	0.38	0.60
−60	1.90	1.44	1.10	0.80	0.55	0.36	0.19	0.11	0.07	0.09	0.16	0.27
−65	1.44	1.04	0.77	0.51	0.32	0.18	0.07	0.03	0.01	0.02	0.04	0.12
−70	0.99	0.73	0.51	0.32	0.19	0.08	0.03	0.01	0.00	0.00	0.01	0.04
−75	0.64	0.49	0.32	0.21	0.12	0.05	0.01	0.00	0.00	0.00	0.00	0.01
−80	0.39	0.28	0.21	0.14	0.07	0.04	0.01	0.01	0.00	0.00	0.00	0.01
−85	0.20	0.18	0.13	0.11	0.07	0.05	0.04	0.03	0.02	0.02	0.03	0.04

Table 17-2. Vertical Cutoff Rigidities (GV) (Contd.)

Geographic latitude	Geographic longitude (E)											
	180	195	210	225	240	255	270	285	300	315	330	345
85	0.02	0.01	0.01	0.01	0.00	0.00	0.00	0.00	0.00	0.00	0.00	0.01
80	0.07	0.05	0.03	0.01	0.00	0.00	0.00	0.00	0.00	0.00	0.01	0.02
75	0.22	0.16	0.09	0.05	0.02	0.00	0.00	0.00	0.00	0.01	0.03	0.06
70	0.51	0.38	0.26	0.14	0.06	0.02	0.01	0.01	0.02	0.05	0.10	0.19
65	1.03	0.84	0.59	0.35	0.20	0.09	0.05	0.04	0.07	0.14	0.29	0.43
60	1.84	1.48	1.06	0.71	0.43	0.24	0.16	0.14	0.19	0.34	0.55	0.85
55	2.95	2.34	1.80	1.27	0.80	0.50	0.36	0.32	0.41	0.66	1.06	1.53
50	4.36	3.62	2.85	2.08	1.45	0.96	0.71	0.63	0.79	1.19	1.81	2.58
45	5.63	4.92	4.22	3.20	2.42	1.73	1.27	1.14	1.35	1.98	2.97	4.01
40	8.05	6.60	5.60	4.68	3.75	2.88	2.14	1.87	2.10	2.96	4.50	5.65
35	9.63	9.21	7.87	6.36	5.38	4.35	3.23	2.82	3.11	4.50	6.06	8.43
30	11.88	10.78	9.90	9.11	7.35	5.83	4.59	3.93	4.24	5.88	8.91	10.46
25	13.29	12.71	12.14	11.37	10.11	8.21	6.24	5.15	5.80	8.44	10.92	12.17
20	14.16	13.68	13.25	12.70	11.89	10.46	8.09	6.99	7.67	10.38	12.40	13.32
15	14.86	14.44	14.08	13.64	13.03	11.84	9.79	7.63	9.26	12.11	13.18	13.90
10	15.37	15.01	14.68	14.31	13.82	12.97	11.71	10.80	11.68	12.87	13.62	14.16
5	15.68	15.37	15.06	14.74	14.34	13.75	12.90	12.33	12.71	13.30	13.79	14.13
0	15.75	15.51	15.24	14.95	14.61	14.17	13.61	13.15	13.14	13.47	13.71	13.84
−5	15.55	15.40	15.19	14.94	14.66	14.31	13.86	13.44	13.31	13.42	13.43	13.34
−10	15.05	15.02	14.90	14.74	14.53	14.25	13.80	13.48	13.26	13.17	12.97	12.66
−15	14.17	14.34	14.37	14.33	14.21	14.01	13.71	13.33	13.02	12.76	12.33	11.62
−20	12.87	13.27	13.57	13.69	13.70	13.61	13.38	13.02	12.64	12.19	11.44	10.43
−25	10.37	11.22	12.11	12.80	13.01	13.05	12.91	12.58	12.11	11.45	10.47	9.03
−30	7.96	9.46	9.54	10.62	12.09	12.33	12.32	12.01	11.44	10.62	9.28	7.73
−35	5.72	6.63	7.93	9.24	9.61	11.40	11.60	11.37	10.63	9.60	8.03	6.73
−40	4.16	4.91	5.59	6.75	8.38	9.64	10.70	10.41	9.73	8.54	7.15	5.93
−45	2.75	3.42	4.31	4.92	5.92	7.87	9.30	9.33	8.60	7.67	6.54	4.79
−50	1.67	2.28	2.97	3.80	4.53	5.61	7.19	8.01	7.67	6.58	5.10	3.96
−55	0.95	1.41	1.94	2.65	3.40	4.32	5.12	5.52	5.50	4.96	4.02	3.27
−60	0.49	0.80	1.24	1.74	2.32	3.07	3.89	4.26	4.24	3.92	3.29	2.50
−65	0.23	0.45	0.73	1.12	1.55	2.08	2.65	2.90	2.94	2.75	2.37	1.86
−70	0.10	0.23	0.41	0.66	0.98	1.31	1.64	1.89	1.97	1.87	1.60	1.31
−75	0.05	0.12	0.24	0.38	0.56	0.77	0.94	1.07	1.17	1.11	1.00	0.83
−80	0.04	0.08	0.15	0.22	0.32	0.42	0.51	0.59	0.62	0.60	0.54	0.48
−85	0.05	0.07	0.11	0.15	0.18	0.20	0.24	0.27	0.28	0.28	0.28	0.23

17.3.3 Charged-Particle Flux Within the Atmosphere

The intensity and composition of the cosmic rays observed within the atmosphere depend, in addition to the cutoff rigidity of the observation point, also on the quantity of absorbing material traversed before observation. The ionization rate measured within the atmosphere depends upon the amount of matter above the point of observation and on its distribution in height. Atmospheric conditions, especially barometric pressure, have an appreciable effect on the measured intensity, hence cosmic-ray intensities are usually reported in terms of atmospheric depth (mass of air per unit area above the observation point) or of air pressure at the observation point rather than the altitude of the observation.

At a given altitude, the value of the pressure in millibars is about 2% less than the atmospheric depth in grams per square centimeter. Figure 17-32 is a plot of atmospheric depth as a function of altitude; for graphs and tables for computing air masses at various zenith angles, see Ely (1962). Figures 17-33 and 17-34 illustrate the variations of cosmic ray intensities with atmospheric depth and with solar activity; ionization rates in the atmosphere are given as a function of atmospheric depth for a ten-year period that includes the solar-cycle minimum in 1954 and the maximum in 1957. Figure 17-35 shows the different ionization rates in the atmosphere at roughly 30-km altitude as a function of north geomagnetic latitude during four different years.

Primary cosmic rays incident upon the top of the earth's atmosphere interact with air nuclei producing high-energy secondary cosmic-rays. These secondary particles, in turn, interact with other nuclei and produce additional secondaries. Figure 17-36 illustrates a nuclear cascade process initiated by a primary cosmic ray. The production of secondary components becomes significant at about 55-km altitude (4-mb pressure) with the local intensity reaching a maximum (the Pfotzer maximum) at approximately 20 km (56 mb). The intensity of secondaries then decreases from the Pfotzer maximum to the surface of the earth as the particles lose energy by additional collisions until the majority either decay or are absorbed.

The particles that comprise the secondary component are primarily π and μ mesons, neutrons, protons, electrons, and γ-ray photons; neutrons and μ mesons are the secondaries most commonly measured on the earth's surface. The secondary cosmic rays are often classified into three major components: the hard component, which is primarily relativistic mesons; the nucleonic component, which is the locally produced protons and neutrons; and the soft component, which is the electrons and the γ rays. Figure 17-37 shows the intensity at solar minimum of fast secondary neutrons at four north-geomagnetic latitudes as a function of atmospheric pressure.

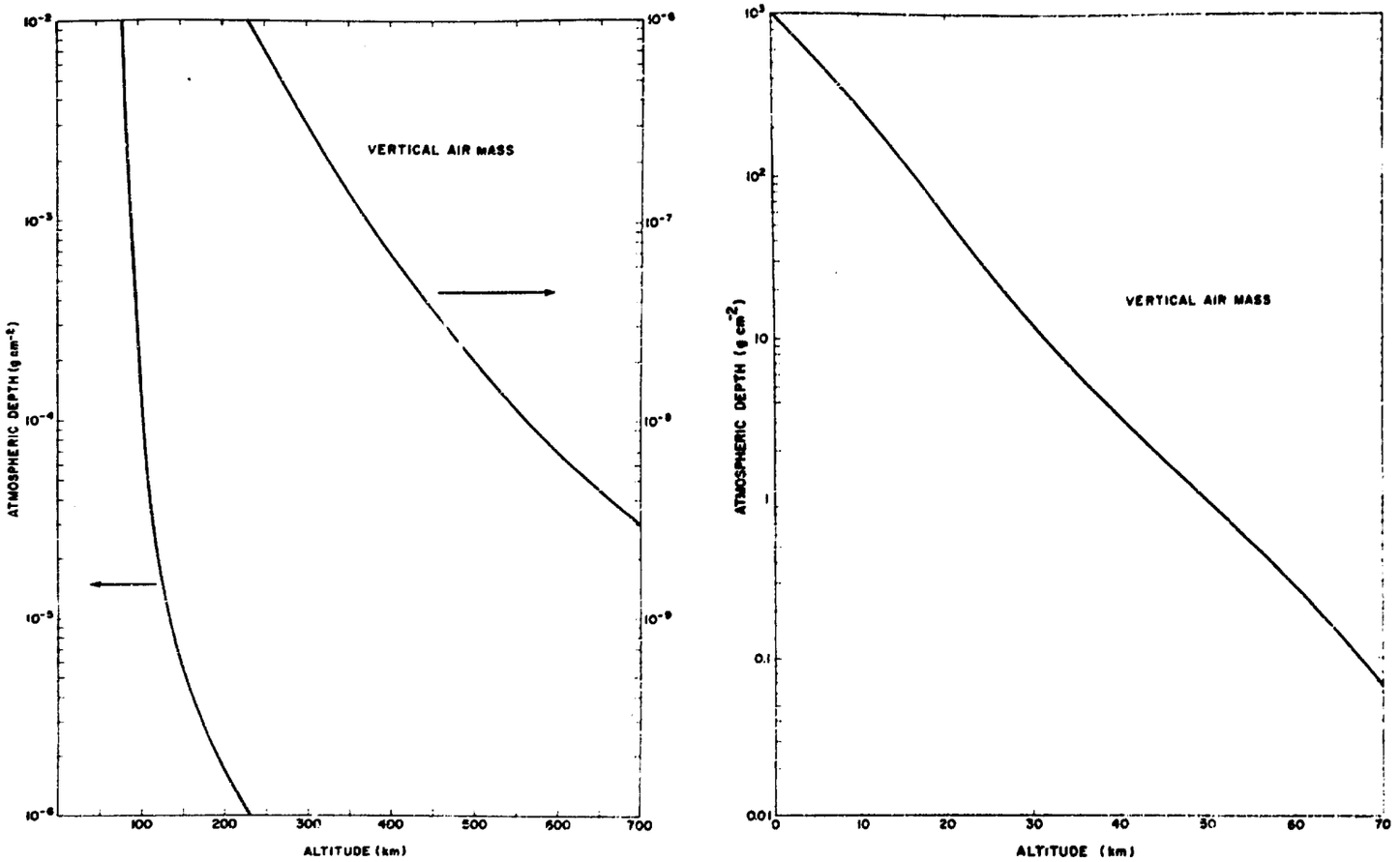

Figure 17-32. The Mass of Air per Unit Area in a Vertical Column Extending Upward from a Height H Above Sea Level. (From Ely, 1962)

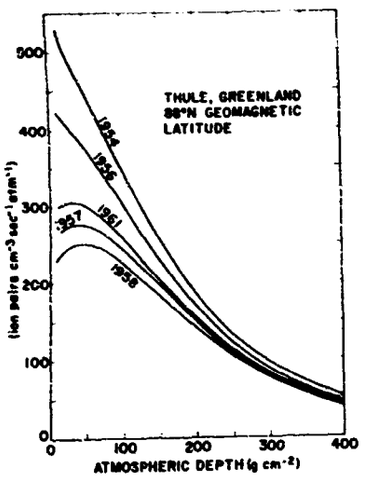

Figure 17-33. Yearly Average of Cosmic Ray Ionization Rate per Atmosphere of Air as a Function of Atmospheric Depth. (From Neher and Anderson, 1962)

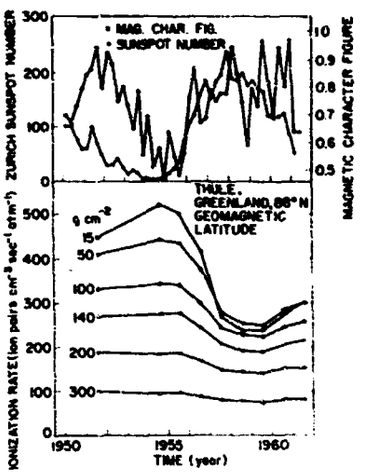

Figure 17-34. Cosmic Ray Ionization Rate per Atmosphere of Air as a Function of Time for Selected Atmospheric Depths. Quarterly Zurich sunspot number and quarterly planetary magnetic character figures are shown for comparison. (From Neher and Anderson, 1962)

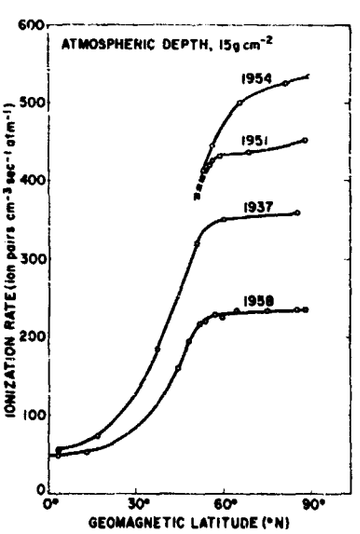

Figure 17-35. Cosmic Ray Ionization Rates per Atmosphere of Air Near the Top of the Atmosphere as a Function of Latitude for Various Years. (From Neher and Anderson 1962)

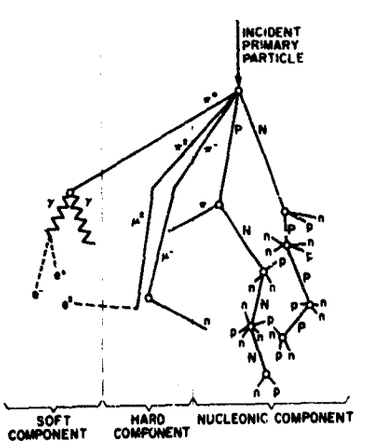

Figure 17-36. Schematic Diagram of a Cosmic Ray Shower. N and P are high energy, n and p disintegration-product, neutrons and protons; pions, mesons, electrons, positrons, and gamma rays are indicated by conventional symbols

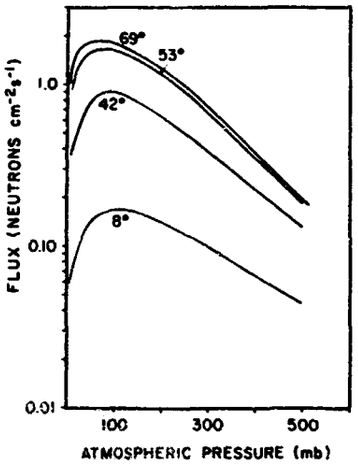

Figure 17-37. Flux of 1 to 10 MeV Neutrons as a Function of Altitude (Atmospheric Pressure) at Various Indicated Latitudes During Solar Minimum. (After Holt, et al, 1966)

In theory, the intensity of any specified secondary component can be derived from a knowledge of the primary spectrum and the specific yield functions, but at present the yield functions are not accurately known. Perhaps the most advanced work on the secondary component is that being done on the atmospheric neutrons. Neutron monitors, which measure the nucleonic component, are advantageous for the study of primary flux variations because they are particularly sensitive indicators of primary radiation, with energies from 500 MeV to a few GeV. The analysis of neutron monitor data provides a great deal of our knowledge of cosmic-ray variations; data for a complete solar cycle (beginning in 1955) have been obtained by a worldwide network of neutron monitors.

17.3.4 Flux Modulations

There is no experimental evidence that the average galactic cosmic-ray intensity has undergone any significant long-period changes. The radioactive isotope C^{14} (5×10^3 yr half-life) is produced in the atmosphere by cosmic rays, and agreements in the dating of archaeological artifacts by the C^{14} method and by archaeological methods imply that any long-period change in the cosmic-ray intensity in the last 30,000 years is smaller than a few percent. The abundance of Be^{10} (2.5×10^6 yr half-life), another cosmic-ray produced isotope, indicates that the mean cosmic-ray intensity has changed by less than a factor of 10 in the past 10^6 years. There are, however, in addition to the variation of intensity during the solar cycle, short-term variations in cosmic-ray intensities.

The variation of cosmic-ray flux with the 11-year solar cycle is indicated by the year to year variations shown in Figures 17-33, 17-34, 17-35, and 17-38.

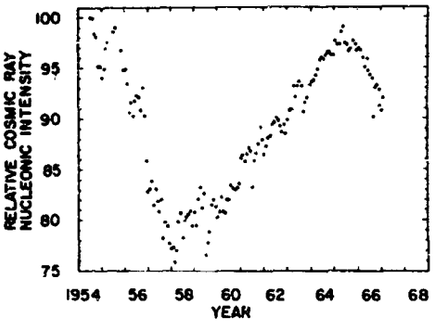

Figure 17-38. Monthly Averages of Relative Intensities Observed by the Neutron Monitor at Mt. Washington, N.H.; Cutoff Rigidity 1.41 GV

An increase in solar activity corresponds to a decrease in galactic cosmic-ray intensity. From solar minimum to solar maximum, the low-energy primary particles tend to be removed from the flux in the vicinity of the earth, decreasing the energy density of these primary galactic cosmic-rays by about 40%. Figure 17-38 illustrates the solar cycle modulation of the cosmic-ray nucleonic intensity observed by the Mt. Washington neutron monitor. The intensity does not change smoothly from maximum to minimum values. It drops sharply and the decrease is followed by a partial recovery. This modulation is thought to be caused by an increase in the extent of the solar-interplanetary magnetic field contained in plasmas that are emitted by the sun in increased amounts during active periods. Changes in cosmic-ray intensity, however, lag changes in sunspot number by 9 to 12 months. As the solar activity increases from minimum, primary particles of increasingly higher energy are affected. Particles with rigidity higher than about 15 GV, however, seem to be relatively unaffected.

Short-term variations can be classified as follows: 27-day variations; 24-hour variations; sudden decreases; and sudden increases. The 27-day variations are related to processes in the solar atmosphere which affect conditions of the interplanetary medium. The 24-hour variations are normally about 0.25%, implying a small diurnal anisotropy. This anisotropy was invariant during the period from 1957 to 1965 while solar activity decreased from maximum (1957) to minimum (1964). The normal state of the diurnal anisotropy is energy independent. The amplitude varies as the cosine of the declination, and the maximum flux (3.8×10^{-3} times the isotropic flux) is incident from a direction 90° to the east of the earth-sun line (McCracken and Rao, 1966). There is also a semi-diurnal anisotropy with an amplitude of approximately 0.1% and maximum 60° to the west of the earth-sun line (Ables, et al, 1966). For detailed discussions of these variations and the variation with geomagnetic disturbances, see Dorman (1963).

Sudden decreases, called Forbush events, are associated with interactions between primary particles and the magnetic fields contained in solar corpuscular streams and interplanetary plasma.

At the onset of a geomagnetic storm (Sec. 11.4), or a few hours after the onset, cosmic-ray intensity may decrease rather sharply for about a day to a minimum that is sometimes more than 10% below the pre-storm value. The intensity then increases rather slowly, generally taking several days to recover, during which time the amplitude of the diurnal variation may be enhanced.

A few decreases in cosmic-ray intensity that are not associated with visual solar flares have been observed during magnetic storms. Conversely, some large geomagnetic storms are not associated with any significant changes in the cosmic-ray intensity. Although during magnetic storms in which the earth's field decreases there is a corresponding decrease in cutoff rigidity, accurate determinations of cutoff rigidities are not available for geomagnetically disturbed periods.

17.4 ENERGETIC SOLAR PARTICLES (SOLAR COSMIC RAYS)

Charged particles emitted sporadically by the sun with energies from a few MeV to a few GeV are described here; the continuous solar emission of charged particles with much lower energies (the solar wind) is described in Chapter 18.

The highest energy particles (above 500 MeV) are emitted only at times of intense solar activity, generally during solar flares of importance 3 or 4. The low energy particles (about 5 to 100 MeV) can be associated with solar flares of importance 2 or greater. Most particle events can be associated with a particular solar flare, but most solar flares do not produce particle events detectable by earth-based sensors.

Sea level events (also called ground level events) indicate the arrival of the highest-energy particles. For example, neutron monitors located on the earth's surface detect the neutrons produced in the atmosphere by incoming charged particles of energy greater than 500 MeV; the 1000 g/cm^2 of atmosphere above the monitors absorbs essentially all particles with less energy (Sec. 17.3.3). Other types of ground-based instruments depend on this absorption for their operation, utilizing the enhanced ionization in the ionosphere to indicate the arrival of charged particles. Riometers, which are sensitive detectors of cosmic radio-noise intensity, reveal the influx into polar regions of protons with energies of about 5 to 100 MeV; the enhanced ionization produced by these protons causes strong absorption of cosmic radio-noise, i.e. a polar cap absorption (PCA) event.

The frequency of occurrence and the intensity of the events vary strongly with the sunspot cycle. As Figure 17-39 shows, the number of PCA events observed during the sunspot minimum was of the order of one per year, whereas during the sunspot maximum the rate of occurrence was roughly one per month. Table 17-3

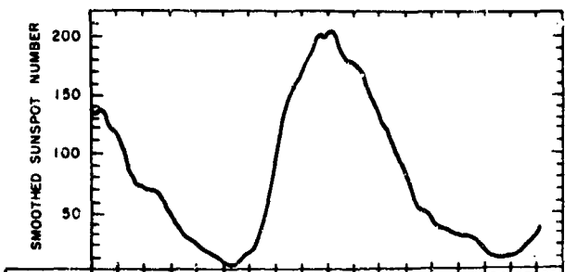

YEAR 19	49	50	51	52	53	54	55	56	57	58	59	60	61	62	63	64	65	66
SEA LEVEL (NEUTRON-MONITOR) EVENTS	1	0	0	0	0	0	0	2	0	0	1	5	2	0	0	0	0	1
PCA EVENTS	6*	4*	4*	0*	2*	0*	1	5	15	12	7	13	7	3	4	1	1	4

*IONOSONDE DATA, SOME EVENTS MAY HAVE BEEN MISSED

Figure 17-39. Number of Solar Particle Events Detected at Sea Level and in the Ionosphere (PCA Events), in Relation to the Solar Cycle. The Sea-Level Events Indicate the Arrival of the Highest Energy (>500 MeV) Solar Particles; PCA Events Indicate the Arrival of Lower Energy (>20 MeV) Solar Particles. (After Fichtel and McDonald, 1967)

describes the large events observed during high solar activity (1956-1961). Table 17-4 lists the most significant events during low solar activity (1962-1966). Many small events were also observed during this period of solar minimum, but a direct comparison with the frequency of small events during the earlier solar maximum cannot be made because the detectors used during the minimum period were much more sensitive than those previously available. The intensities and durations of the solar disturbances vary so much, and the interplanetary medium between the sun and the earth is so variable, that there is a little value in constructing hypothetical models of an "average" solar cosmic-ray event. This discussion is limited to describing the parameters used to characterize events and to indicating the observed limits of these parameters.

An energetic solar-particle event may be characterized by the following parameters:

(1) particle types present;

(2) intensity (generally the number of particles per unit area per second with energy above a specified value);

(3) energy spectrum or rigidity spectrum;

(4) rise time and decay time;

(5) degree of anisotropy and its direction; and

(6) volume of interplanetary space over which the flux extends.

Table 17-3. Some Major Solar Cosmic Ray Observations During 1956-1961. (After McDonald 1963).

		Solar Flare Data			Cosmic Ray Data							
					Onset to Max. Time (h)		Decay Time (h)		Peak Flux (no. cm^{-2} sec^{-1})		Integrated • Intensity (no. cm^{-2})	
	Date	Importance	Heliographic Position (deg)	Optical Maximum (UT)	>30 MeV	>100 MeV	>30 MeV	>100 MeV	>30 MeV	>100 MeV	>30 MeV	>100 MeV
1956	Feb 23	3+	N22 W74	0340	6-8	3-4	30	16	6,200	5,000	6.5×10^8	3.2×10^8
1957	Jan 20	3+	S25 W30	1120					2,000-3,000	100-200	3×10^8	10^7
	Mar 23	3+	S14 E78	1005			(40)	(20)	1,200-1,500	≈ 50	2×10^8	5×10^6
	Jul 7	3+	N25 W08	0115			32	16-20	1,500-2,000	≈ 80	3×10^8	7×10^6
1958	Aug 16	3+	S14 W50	0440	10		18		200		2×10^7	
	Aug 22	3	N18 W10	1448	10-12	3-4	20	8-12	500	20	5×10^7	1×10^6
	Aug 26	3	N20 W54	0027	≈ 9		(12)		1,100		5.3×10^7	
	May 10	3+	N23 E47	2118	18-22	12-18	22	10-14	6,000-8,000	1,000	7×10^8	7.5×10^7
1959	Jul 10	3+	N22 E70	0222	30-40	18-20	40	20	4,000	1,200	8.8×10^8	1.0×10^8
	Jul 14	3+	N16 E07	0349	16-20	12-18	18	9-12	10,000-12,000	1,200	1.1×10^9	6.3×10^7
	Jul 16	3+	N08 W26	2145	12-14	4-5	30	18	16,000-18,000	1,500	8.1×10^8	1.3×10^8
	Apr 1	3	N12 W10	0859	2-3	< 1	12	4-6	50	6	2.7×10^6	1.5×10^5
	Apr 5	2+	N10 W61	0245			12		40		2×10^6	
	Apr 28	3	S05 E34	0130	8-10	3-4	18 24	8	300	20	2.5×10^7	7×10^5
	May 4	3+	N14 W90	1020	2-3	< 1	8	4	200	40	7×10^6	7×10^5
1960	Sep 3	3	N18 E88	0110	12-16	7-9	32	26	240	60	4×10^7	7×10^6
	Nov 12	3+	N27 W02	1329	12-16	8-10	18-24	14-18	12,000	2,500	1.4×10^9	3.5×10^8
	Nov 15	3+	N30 W32	0221	10-16	3-5	16-20	8-12	6,000	2,400	5.2×10^8	1.2×10^8
	Nov 20	3	N28 W113	2020	3-4	≈ 1	10-16	4-6	1,000	400	6×10^7	6×10^6
	Jul 11	3	S06 E32	1700	8-10	4	22-26	18	20	3	2×10^6	3×10^5
	Jul 12	3+	S07 E22	1030	8-12	6	16-20	12	120	15	1.0×10^8	1.6×10^6
1961	Jul 18	3+	S06 W60	1010	6-10	2-3	24	12	2,500	600	2.1×10^8	4.8×10^7
	Jul 20	3+	S07 W90	(1600)	4-6	1.5	6-8	3	300	70	9×10^6	1.2×10^6
	Sep 28	3	N14 E30	2223							2.2×10^5	9.7×10^4

• Values tend to be overestimated.

Table 17-4. Principal Solar Cosmic-Ray Events 1962-1966

Date	Importance Class	Time of Optical Flare (h)	Heliographic Position (deg)	Peak Flux Protons >20 MeV (no. $cm^{-2}s^{-1}$)
1962 Feb 20*	2	1222	N10 E79	0.5
1963 Sep 20	2	2255	N10 W09	4
1964 Mar 16	2	1550	N05 W75	0.7
1965 Feb 5	2	1750	N07 W25	50
Oct 4	2	0938	S20 W29	3
1966 Mar 24	3B	0233	N18 W37	15
Jul 7	2B	0022	N34 W45	30
Aug 28	2B	1530	N08 W03	15

*A number of flares occurred on this date; data listed correspond to the first flare occurrence.

Unfortunately, these parameters do not remain constant from event to event and even change during a single event. The rise and decay times tend to be shorter for higher-energy particles than for lower-energy ones, so that generally the spectra become steeper at later times in an event. It is convenient to give the time history of particles above a specified threshold energy; because of the steepness of solar-particle spectra, this is essentially the time history of the particles at the specified energy. Table 17-3 gives an indication of the time histories for 30 MeV and 100 MeV protons for a number of large events.

17.4.1 Composition

Solar cosmic-ray events are often referred to as solar proton events. Although protons are the major component, significant numbers of alpha particles are observed. The rigidity spectra of protons and alphas tend to be similar, but the relative proportion of particles varies considerably between events and even during a given event. Within a given rigidity interval an alpha-to-proton ratio as high as 1 has been reported, whereas in some events very few alpha particles have been detected. This variable alpha-to-proton ratio is one of the most puzzling aspects of solar cosmic-rays. Too little is known at this time to discuss the abundance of the various hydrogen and helium isotopes. A rough estimate for the deuteron-to-proton and the triton-to-proton ratio in the energy interval 10 to 100 MeV/nucleon is of the order 10^{-3} or less.

Table 17-5. Estimated Relative Abundances (By Number Based on 1.0 for Oxygen) of Solar Particles Compared with Galactic Cosmic Rays. (After Fichtel and McDonald, 1967).

Element	Solar			Galactic
	Cosmic Rays	Photosphere	Corona	Cosmic Rays
He	107 ± 14	?	445	48
Li	-	$<10^{-5}$	-	0.3
Be-B	<0.02	$<10^{-5}$	-	0.8
C	0.59 ± 0.07	0.6	1.3	1.8
N	0.19 ± 0.04	0.1	0.1	$\lesssim$0.8
O	1.0	1.0	1.0	1.0
F	<0.03	0.001	-	$\lesssim$0.1
Ne	0.13 ± 0.02	?	0.11	0.30
Na	-	0.002	0.01	0.19
Mg	0.043 ± 0.011	0.027	0.20	0.32
Al	-	0.002	0.01	0.06
Si	0.033 ± 0.011	0.035	0.22	0.12
P-Sc	0.057 ± 0.017	0.032	-	0.13
Ti-Ni	$\lesssim$0.02	0.006	~0.1	0.28

Nuclei with charge greater than 2 have recently been observed in a number of events. (During the 1954-1964 solar cycle, experimental techniques were not adequate to establish or rule out their presence.) The rigidity spectra observed tend to be similar to those of the protons and alpha particles. Table 17-5 gives the best available data on the relative abundances. The relative abundance of elements in the solar cosmic rays is closer to that of the solar photosphere than to that of galactic cosmic rays. The absence of lithium, beryllium, and boron in the solar particles is consistent with their low universal abundance. The admixture of all elements heavier than helium is about 1 to 2% of the helium component. Apparently, the abundance ratio of heavier elements to helium is reasonably constant as a function of particle rigidity.

The electron component is of particular interest because it provides a possible explanation for the observed radio emission from active flare regions (Sec. 16.3.5). Calculations (Stein and Ney, 1963) satisfactorily explain the radio noise as synchrotron radiation from electrons with flux and initial rigidity-spectrum similar to that observed for protons. Observed fluxes of higher-energy electrons are rather weak although relatively high intensity fluxes of low-energy electrons are observed. A number of electron events with an apparent absence of protons have been detected.

17.4.2 Intensity and Spectra

In the largest events associated with solar flares, the flux of particles near the earth with energy greater than 30 MeV exceeded 10^3 particles $cm^{-2}s^{-1}$ for a

Table 17-6. Large Events During the Period 1956 through 1961. (After Fichtel and McDonald, 1967).

Events (no.)	Integrated Flux E > 30 MeV (particles $cm^{-2}s^{-1}$)
10	10^7 to 10^8
10	10^8 to 10^9
2	$> 10^9$

period of more than a day. The total number of particles arriving at the earth during such events exceeded the total yearly flux of galactic cosmic rays. Table 17-6 gives the size distribution of the largest events observed from 1956 through 1961.

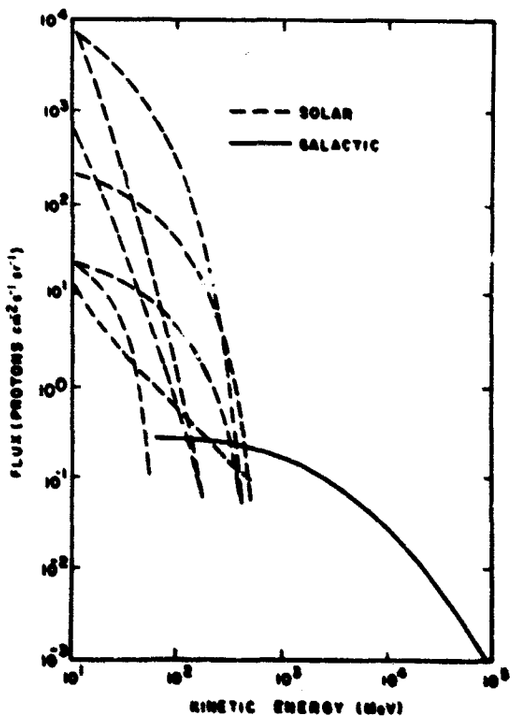

Figure 17-40. Energy Spectra of Protons from Several Moderate-Size Solar Events Compared with the Galactic Cosmic Ray Spectrum at Solar Minimum. (From Fichtel and McDonald, 1967)

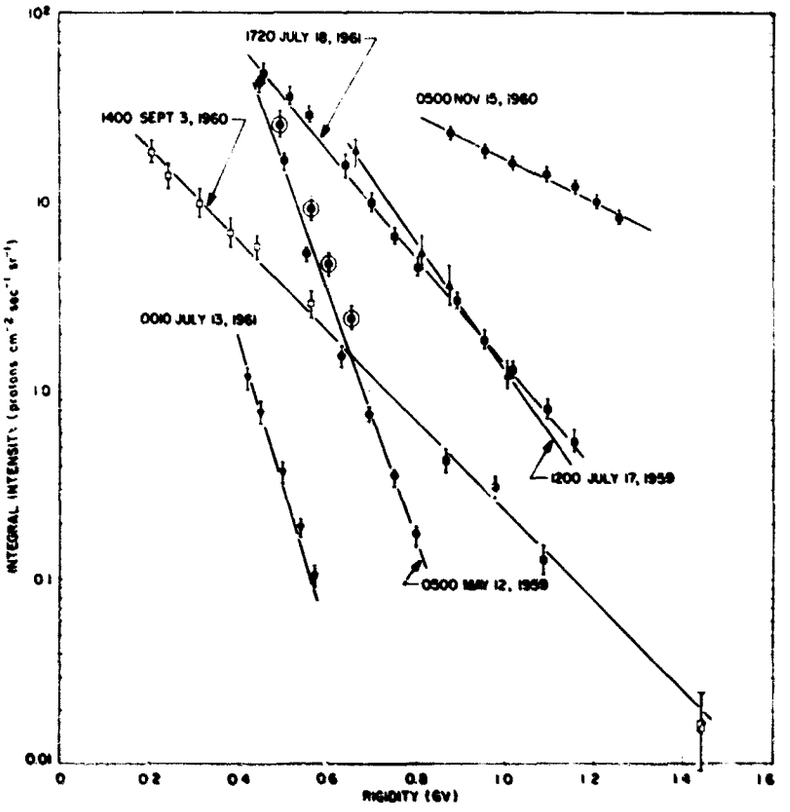

Figure 17-41. Integral Proton Intensity as a Function of Rigidity at Selected Times. Data points taken from counter ascents are shown as solid symbols; those taken with emulsions, as open symbo's. The time of observation is shown for each spectrum; the time of flares is given in Table 17-3. (From Freier and Webber, 1963)

Because both the rise and decay times of the particles vary with energy, the energy spectrum is time-dependent. Solar cosmic rays contain fewer extremely high energy particles, and therefore have steeper spectra than the galactic cosmic rays. Figure 17-40 presents a number of solar particle spectra in comparison to the galactic cosmic-ray spectrum. Reasonably successful attempts have been made to express the time change in the differential rigidity spectrum by the equations of the form:

$$J(P) = J_o(t) \exp [-P/P_o(t)] \qquad (17\text{-}22)$$

P_o is normally in the range 40-400 MV and decreases with time from the beginning of the event. Figure 17-41 shows some exponential rigidity spectra observed during various times within six events.

17.4.3 Anisotropy

Anisotropy of solar-produced particles is related most strongly to the storage and propagation properties of the magnetic fields in interplanetary space. Although data are still too rudimentary to uniquely determine details of the processes involved, a broad model has developed.

Analyses of the results from the neutron-monitor network show that early in the large events the solar particles with energies greater than 500 MeV/nucleon are generally anisotropic. Later on, however, the flux becomes isotropic, which suggests a temporary storage of particles in space near the earth. During the anisotropic phase, the particles appear to arrive at the earth from a preferential direction approximately 50 degrees west of the earth-sun line. This is consistent with the concept of particles flowing away from the sun in paths along solar magnetic field lines which have an Archimedes spiral (garden hose) configuration (see Chapter 18). This is also consistent with the observations of optical flares associated with solar cosmic-ray events on the earth; these flares are located more frequently in the western hemisphere of the solar disk.

Measurements from satellites and probes of solar particles with energies from 1 to 70 MeV and of interplanetary magnetic fields show that within the general spiral shape the magnetic fields also have a finer, filamentary form which normally contains some irregularities. These filaments move with the solar wind and constrain the lower energy particles to move along the filamentary paths. At these lower energies the particle flux can be highly anisotropic for periods up to 48 hours. Major changes in direction, which are related to changes in the magnetic field, occur from hour to hour. One of the implications of these observations is that there is some restriction on the spatial extent of the solar particle propagation. Very little direct evidence is available, but it appears that somewhat less than half the inner solar system is populated by solar cosmic-ray particles during any one event.

17.5 REFERENCES

Anand, K.C., R.R. Daniel, S.A. Stephens, B. Bhowmik, C.S. Krishna, P.K. Aditya, and R.K. Puri, "Rigidity Spectrum of Cosmic-Ray Helium Nuclei ≥ 12 GV", Canadian Journal of Physics, v. 46, p. S652, 1968.

Ables, J.G., K.G. McCracken, and U.R. Roa, "The Semi-diurnal Anisotropy of the Cosmic Radiation", Proceedings, Ninth International Conf. on Cosmic Rays, (London, 1965), v. 1, p. 208, Institute of Physics and Physical Society, London, 1966.

Blanchard, R.C. and W.N. Hess, "Solar Cycle Changes in Inner Zone Protons", J. Geophys. Res., v. 69, no. 19, p. 3927, 1964.

Brown, W. L., "Observations of the Transient Behavior of Electrons in the Artificial Radiation Belts", Radiation Trapped in Earth's Magnetic Field, p. 610, B. M. McCormac, ed., D. Reidel Publishing Co., Dordrecht-Holland, 1966.

Chang, D. P., "Some Plasma Instabilities of the Magnetosphere", Radiation Trapped in Earth's Magnetic Field, p. 491, B. M. McCormac, ed., D. Reidel Publishing Co., Dordrecht-Holland, 1966.

Cornwall, J. M., A. R. Sims and R. S. White, "Atmospheric Density Experienced by Radiation Belt Protons", J. Geophys. Res., v. 70, no. 13, p. 3099, 1965.

Davis, L. R. and J. M. Williamson, "Outer Zone Protons", Radiation Trapped in Earth's Magnetic Field, p. 213, B. M. McCormac, ed., D. Reidel Publishing Co., Dordrecht-Holland, 1966.

Dorman, L. I., Progress in Elementary Particle and Cosmic Ray Physics VII, J. G. Wilson and S. A. Worthuysen, eds., North-Holland Publishing Co., Amsterdam, 1963.

Dragt, A. J., M. M. Austin and R. S. White, "Cosmic Ray and Solar Proton Albedo Neutron Decay Injection", J. Geophys. Res., v. 71, no. 5, p. 1293, 1966.

Dungey, J. W., "Effects of Electromagnetic Perturbations on Particles Trapped in the Radiation Belts", Space Science Reviews, v. 4, p. 199, D. Reidel Publishing Co., Dordrecht-Holland, 1965.

Ely, J. T. A., "Atmospheric Depth and Effective Solid Angle for Radiation Penetrating the Atmosphere", Geophysical Research Papers No. 74 (AFCRL-62-260), Air Force Cambridge Research Laboratories, 1962.

Fichtel, C. E. and F. B. McDonald, "Energetic Particles from the Sun", Annual Review of Astronomy and Astrophysics, v. 5, p. 351, Annual Reviews, Inc., Palo Alto, Calif., 1967.

Fillius, R. W. and C. E. McIlwain, "Anomalous Energy Spectrum of Protons in the Earth's Radiation Belt", Phys. Rev. Letters, v. 12, no. 22, p. 609, 1964.

Filz, R. C. "Observations of Inner Zone Protons in Nuclear Emulsions 1961 to 1966", Earth's Particles and Fields, p. 15, B. M. McCormac, ed., Reinhold Book Corp., 1968.

Filz, R. C., "Comparison of the Low-Altitude Inner-Zone 55-MeV Trapped Proton Fluxes Measured in 1965 and 1961-1962", J. Geophys. Res., v. 72, no. 3, p. 959, 1967.

Filz, R. C. and E. Holeman, "Time and Altitude Dependence of 55-MeV Trapped Protons, August 1961 to June 1964", J. Geophys. Res., v. 70, no. 23, p. 5807, 1965.

Frank, L. A. "Inward Radial Diffusion of Electrons of Greater Than 1.6 Million Electron Volts in the Outer Radiation Zone", J. Geophys. Res., v. 70, no. 15, p. 3533, 1965.

Freden, S. C., J. B. Blake and G. A. Paulikas, "Spatial Variation of the Inner Zone Trapped Proton Spectrum", J. Geophys. Res., v. 70, no. 13, p. 3113, 1965.

Freden, S. C. and G. A. Paulikas, "Trapped Protons at Low Altitudes in the South Atlantic Magnetic Anomaly", J. Geophys. Res., v. 69, no. 7, p. 1259, 1964.

Freier, P. S. and W. R. Webber, "Exponential Rigidity Spectrums for Solar Flare Cosmic Rays", J. Geophys. Res., v. 68, no. 6, p. 1605, 1963.

Garmire, G., "Geomagnetically Trapped Protons with Energies Greater Than 350 MeV", J. Geophys. Res., v. 68, no. 9, p. 2627, 1963.

Gloeckler, G. and J.R. Jokipii, "Solar Modulation and the Energy Density of Galactic Cosmic Rays", Astrophys. J., v. 148, no. 1, part 2, p. L41, 1967.

Heckman, H.H. and G.H. Nakano, "Direct Observations of Mirroring Protons in the South Atlantic Anomaly", Space Research V, p. 329, D.G. King-Hele, P. Muller, and G. Righini, eds., North-Holland Publishing Co., Amsterdam, 1965.

Holt, S.S., R.B. Mendell and S.A. Korff, "Fast Neutron Latitude Variations in the Atmosphere at Solar Minimum", J. Geophys. Res., v. 71, no. 21, p. 5109, 1966.

Imhof, W.L. and R.V. Smith, "The Behavior of Trapped Electrons and Protons at the Lower Edge of the Inner Radiation Belt", J. Geophys. Res., v. 71, no. 17, p. 4157, 1966.

Katz, L., D. Smart, F.R. Paolini, R. Giacconi, and R.J. Talbot, Jr., "Measurements on Trapped Particles Injected by Nuclear Detonations", Space Research IV, p. 646, P. Muller, ed., North-Holland Publishing Co., Amsterdam, 1964.

Kennel, C.F. and H.E. Petschek, "Limit on Stably Trapped Particle Fluxes", J. Geophys. Res., v. 71, no. 1, p. 1, 1966.

L'Heureux, J., "The Primary Cosmic-Ray Electron Spectrum Near Solar Minimum", Astrophys. J., v. 148, no. 2, part 1, p. 399, 1967.

Lindstrom, P.J. and H.H. Heckman, "B-L Space and Geomagnetic Field Models", Lawrence Radiation Laboratory, UCRL-17492, 19 September 1967.

McCracken, K.G. and U.R. Rao, "A Survey of the Diurnal Anisotropy", Proceedings, Ninth International Conf. on Cosmic-Rays, (London, 1965), v. 1, p. 213, Institute of Physics and Physical Society, London, 1966.

McCracken, K.G., U.R. Rao, B.C. Fowler, M.A. Shea and D.F. Smart, "Cosmic Ray Tables", IQSY Instruction Manual No. 10, IQSY Committee, London, 1965.

McDonald, F.R., ed., Solar Proton Manual, National Aeronautics and Space Administration Technical Report, NASA TR R-169, 1963.

McIlwain, C.E., "Ring Current Effects on Trapped Particles", J. Geophys. Res., v. 71, no. 15, p. 3623, 1966.

McIlwain, C.E., "Redistribution of Trapped Protons During a Magnetic Storm", Space Research V, p. 374, D.G. King-Hele, P. Muller, and G. Righini, eds., North-Holland Publishing Co., Amsterdam, 1965.

McIlwain, C.E., "The Radiation Belts, Natural and Artificial," Science, v. 142, p. 355, 1963.

McIlwain, C.E., "Coordinate for Mapping the Distribution of Magnetically Trapped Particles", J. Geophys. Res., v. 66, no. 11, p. 3681, 1961.

Neher, H.V. and H.R. Anderson, "Cosmic Rays at Balloon Altitudes and the Solar Cycle", J. Geophys. Res., v. 67, no. 4, p. 1309, 1962.

Paolini, F.R. and G.C. Theodoridis, "A Study of Energetic Electrons in the Radiation Belts with Hitch Hiker 1", Annales de Geophysique, v, 23, no. 2, p. 2312, 1967.

Pfitzer, K., S. Kane and J.R. Winckler, "The Spectra and Intensity of Electrons in the Radiation Belts", Space Research VI, p. 702, R.L. Smith-Rose, ed., Spartan Books, 1966.

Roederer, J.G., "On the Adiabatic Motion of Energetic Particles in a Model Magnetosphere", J. Geophys. Res., v. 72, no. 3, p. 981, 1967.

Shea, M.A., D.F. Smart, K.G. McCracken, and U.R. Rao, "Supplement to IQSY Instruction Manual No. 10 Cosmic Ray Tables: Asymptotic Directions, Variational Coefficients and Cutoff Rigidities", Special Reports No. 71 (AFCRL-68-0030), Air Force Cambridge Research Laboratories, 1968a.

Shea, M.A., D.F. Smart and J.R. McCall, "A Two Degree by Fifteen Degree World Grid of Trajectory Determined Vertical Cutoff Rigidities", Canadian Journal of Physics, v. 46, p. S1098, 1968b.

Singer, S.F. and A.M. Lencheck, "Geomagnetically Trapped Radiation", Progress in Elementary Particle and Cosmic Ray Physics VI, p. 245, J.G. Wilson and S.A. Worthuysen, eds., North Holland Publishing Co., Amsterdam, 1962.

Smalley, V.G., D.F. Smart and R.C. Filz, "Corpuscular Radiation Environment of a Low Altitude Polar-Orbiting Earth Satellite - A Brief Summary", Air Force Surveys in Geophysics No. 185 (AFCRL-66-540), Air Force Cambridge Research Laboratories, 1966.

Stein, W.A. and E.P. Ney, "Continuum Electromagnetic Radiation from Solar Flares", J. Geophys. Res., v. 68, no. 1, p. 65, 1963.

Stone, E.C., "Physical Significance and Application of L, B_o, and R_o to Geomagnetically Trapped Particles", J. Geophys. Res., v. 68, no. 14, p. 4157, 1963.

Van Allen, J.A., "Spatial Distribution and Time Decay of the Intensities of Geomagnetically Trapped Electrons from the High Altitude Nuclear-Burst of July 1962", Radiation Trapped in Earth's Magnetic Field, p. 575, B.M. McCormac, ed., D. Reidel Publishing Co., Dordrecht-Holland, 1966.

Vette, J.I., "A Model Proton Environment Above 4 MeV" Radiation Trapped in Earth's Magnetic Field, p. 865, B.M. McCormac, ed., D. Reidel Publishing Co., Dordrecht-Holland, 1966.

Vette, J.I., A.B. Lucero, and J.A. Wright "Models of the Trapped Radiation Environment, Volume II: Inner and Outer Zone Electrons", National Aeronautics and Space Administration, NASA SP-3024, 1966.

Walt, M., "Loss Rates of Trapped Electrons by Atmospheric Collisions", Radiation Trapped in Earth's Magnetic Field, p. 337, B.M. McCormac, ed., D. Reidel Publishing Co., Dordrecht-Holland, 1966.

Walt, M. and L.L. Newkirk, "Addition to Investigation of the Decay of the Starfish Radiation Belt", J. Geophys. Res., v. 71, no. 13, p. 3265, 1966.

West, H.I., "Some Observations of the Trapped Electrons Produced by the Russian High Altitude Nuclear Detonation of October 28, 1962", Radiation Trapped in Earth's Magnetic Field, p. 634, B.M. McCormac, ed., D. Reidel Publishing Co., Dordrecht-Holland, 1966.

Unclassified
Security Classification

DOCUMENT CONTROL DATA - R&D

(Security classification of title, body of abstract and indexing annotation must be entered when the overall report is classified)

1. ORIGINATING ACTIVITY (Corporate author)
Air Force Cambridge Research Laboratories (ECS)
L. G. Hanscom Field
Bedford, Massachusetts 01730

2a. REPORT SECURITY CLASSIFICATION
Unclassified

2b. GROUP

3. REPORT TITLE
CORPUSCULAR RADIATION: A REVISION OF CHAPTER 17, HANDBOOK OF GEOPHYSICS AND SPACE ENVIRONMENTS

4. DESCRIPTIVE NOTES (Type of report and inclusive dates)
Scientific. Summary through June, 1968.

5. AUTHOR(S) (First name, middle initial, last name)
R. C. Filz G. A. Kuck D. F. Smart
L. Katz M. A. Shea

6. REPORT DATE	7a. TOTAL NO. OF PAGES	7b. NO. OF REFS
December 1968	62	52

8a. CONTRACT OR GRANT NO.	9a. ORIGINATOR'S REPORT NUMBER(S)
b. PROJECT, TASK, WORK UNIT NOS. None	AFCRL-68-0666
c. DOD ELEMENT	9b. OTHER REPORT NO(S) (Any other numbers that may be assigned this report)
d. DOD SUBELEMENT	AFSG No. 208

10. DISTRIBUTION STATEMENT
1-Distribution of this document is unlimited. It may be released to the Clearinghouse, Department of Commerce, for sale to the general public.

11. SUPPLEMENTARY NOTES	12. SPONSORING MILITARY ACTIVITY
TECH, OTHER	Air Force Cambridge Research Laboratories (ECS) L. G. Hanscom Field Bedford, Massachusetts 01730

13. ABSTRACT

This survey is a summary of available information on the corpuscular radiation environment in the vicinity of the earth and in the earth's atmosphere; radiation trapped in the magnetosphere (Van Allen belts), galactic cosmic rays, and high-energy solar particles (solar cosmic rays) are described. The topics presented are: the motions of charged particles in the geomagnetic field; the spatial and temporal distributions, intensities, and energies of electrons and protons trapped in the earth's magnetic field; the composition, intensity, energy spectrum and variations of galactic cosmic rays; and the composition, intensities, anisotropy, and variations of the high-energy charged-particles emitted sporadically by the sun in association with solar flares and other solar disturbances.

DD FORM 1 NOV 68 1473

Unclassified
Security Classification

14. KEY WORDS	LINK A		LINK B		LINK C	
	ROLE	WT	ROLE	WT	ROLE	WT
Cosmic Rays Environmental High-energy Charged-particles Solar Cosmic Rays Trapped Particles in Magnetosphere Van Allen Zones						